SANDIA REPORT

SAND91—1061 • UC—600
Unlimited Release
Printed June 1991

General Implementation of Thin-Slot Algorithms into the Finite-Difference Time-Domain Code, TSAR, Based on a Slot Data File

Douglas J. Riley, C. David Turner

Prepared by
Sandia National Laboratories
Albuquerque, New Mexico 87185 and Livermore, California 94550
for the United States Department of Energy
under Contract DE-AC04-76DP00789

Issued by Sandia National Laboratories, operated for the United States Department of Energy by Sandia Corporation.

Available to DOE and DOE contractors from
Office of Scientific and Technical Information
PO Box 62
Oak Ridge, TN 37831

Prices available from (615) 576-8401, FTS 626-8401

Available to the public from
National Technical Information Service
US Department of Commerce
5285 Port Royal Rd
Springfield, VA 22161

NTIS price codes
Printed copy: A05
Microfiche copy: A01

SAND--91-1061

DE91 014336

SAND91–1061
Unlimited Release
Printed June, 1991

GENERAL IMPLEMENTATION OF THIN–SLOT ALGORITHMS INTO THE FINITE–DIFFERENCE TIME–DOMAIN CODE, TSAR, BASED ON A SLOT DATA FILE

Douglas J. Riley and C. David Turner

Radiation and Electromagnetic Analysis Division
Sandia National Laboratories
Albuquerque, NM 87185

ABSTRACT

Two methods for modeling arbitrary narrow apertures in finite-difference time-domain (FDTD) codes are presented in this paper. The first technique is based on the hybrid thin-slot algorithm (HTSA) which models the aperture physics using an integral equation approach. This method can model slots that are narrow both in width and depth with regard to the FDTD spatial cell, but is restricted to planar apertures. The second method is based on a contour technique that directly modifies the FDTD equations local to the aperture. The contour method is geometrically more flexible than the HTSA, but the depth of the aperture is restricted to the actual FDTD mesh. A technique to incorporate both narrow-aperture algorithms into the FDTD code, TSAR, based on a "slot data file" is presented in this paper. Results for a variety of complex aperture contours are provided, and limitations of the algorithms are discussed.

LIST OF CONTENTS

LIST OF FIGURES

LIST OF SYMBOLS

Symbol	Definition
c	Speed of light in vacuum (m/s)
ϵ_0	Free-space permittivity (F/m)
μ_0	Free-space permeability (H/m)
η_0	Free-space impedance (Ohms)
σ_g	Conductivity of slot gasket (S/m)
ϵ_g	Permittivity of slot gasket (F/m)
t	Time (s)
a	Equivalent radius for slot (m)
w	Width of slot (m)
d	Depth of slot (m)
K_s	Magnetic current along slot (V)
L	Effective length of the slot (m)
G	Half-space Green's function for slot
f	Frequency (Hz)
Δ_x	FDTD spatial delta in x (m)
Δ_y	FDTD spatial delta in y (m)
Δ_z	FDTD spatial delta in z (m)
Δt	FDTD time delta (s)
Δt_s	HTSA time delta (s)
$\mathbf{E}$	FDTD electric field (V/m) (Bold font)
$\mathbf{H}$	FDTD magnetic field (A/m) (Bold font)
$\bar{E}$	Electric field for isolated slot problem (V/m)

Symbol	Definition
$\bar{H}$	Magnetic field for isolated slot problem (A/m)
$\bar{\mathscr{H}}$	Magnetic field radiated by magnetic current into empty half space (A/m)
Λ	Piecewise linear (triangular) basis function for HTSA
λ	Free-space wavelength (m)
τ	Retarded time for HTSA (s)
$Z_{in_{slot}}$	Input impedance for a slot (Ohms)

ACKNOWLEDGMENTS

The authors acknowledge Lt. Tom Timmerman of the Phillips Laboratory for his interest and support to pursue the work reported here. Special thanks to Dr. Scott Ray of the Lawrence Livermore National Laboratory for providing the TSAR code and also for providing guidance on its design details, to Dr. Larry Bacon of Sandia National Laboratories for providing the moment-method code that models slots with depth which was used to obtain some of the results presented in this paper, and to Dr. Gary Scrivner of Sandia National Laboratories for helpful discussions.

1. INTRODUCTION

Finite-difference time-domain (FDTD) codes are used to directly solve the transient form of Maxwell's equations in three-dimensional space. The fundamental algorithm that these codes generally follow is due to Yee [1]. The traditional Yee algorithm is based on a cartesian coordinate system that staggers electric- and magnetic-field components in both space and time. This offset enables FDTD codes to yield good results with as few as five to ten cells per wavelength, compared to 40 (or more) cells per wavelength often required by traditional method-of-moments codes that solve the electric- or magnetic-field integral equations.

The FDTD method is well suited to three-dimensional problems involving conducting and/or dielectric materials, with diverse applications ranging from aircraft analysis to hyperthermia [2–5]. Because it is fundamentally a volumetric method, anisotropic materials can also be directly accommodated.

Although the wide range of problems that FDTD can address is encouraging, two fundamental limitations restrict its use: 1) Just as the volumetric nature of the method opens new applications on one hand, the computer resources required to actually solve the problem can rapidly become prohibitive for even the most powerful machines; and 2) The cartesian nature of the method restricts the level of surface detail that can be accurately modeled.[1]

To limit computer resource requirements, the spatial sampling size is often forced to be chosen larger than what one would actually desire. Although the problem size may now be tractable, the level of detail that can be modeled as well as the usable upper frequency content of the results is limited. Consequently, important system features, such as apertures, are often ignored in large system studies simply because

[1]This is not as serious a problem for radar cross-section calculations as for aperture-physics studies and/or detailed surface-current analyses.

they cannot be resolved. The successful resolution of very narrow apertures within the FDTD code, TSAR (Temporal Scattering And Response [5]) is the purpose of this study.

Four methods to resolve apertures that are less than the FDTD spatial cell in width have been discussed in the literature: 1) An "In-Cell" capacitance method by Gilbert and Holland [6]; 2) A contour method that directly modifies the FDTD equations local to slot described by Taflove, *et al.* [7], and also by Merewether and Fisher [8], and Cho and Merewether [9]; 3) A sub-gridding method that reduces the FDTD spatial cell size local to the aperture [10]; and 4) An integral-equation method known as the Hybrid Thin-Slot Algorithm (HTSA) [11]. The HTSA, and a contour method based on defining conducting walls on tangential $\overline{E}$ fields (E-wall Thin-Slot Formalism, or ETSF), are the methods described in this report and incorporated in TSAR.[2]

Neither the HTSA nor the ETSF provide universal solutions to the narrow slot problem, but each has merits appropriate for particular applications. The HTSA is restricted to planar slots, but can solve the important case that *both* the width and depth of the slot are narrow compared to the FDTD spatial cell. In addition, the HTSA is not bound to the FDTD discrete spatial and time increments, and therefore, high-resolution solutions for the slot physics are possible. The ETSF, on the other hand, can accommodate non-planar slots, but the slot depth is restricted to the actual FDTD wall gridding. A *caveat* for ETSF application to non-planar slots, i.e., those on a stair-stepped wall, is that these slots do not have their depths and lengths well defined, and therefore, the results are of only limited accuracy.

---

[2]An alternative contour method that defines walls on tangential $\overline{H}$ fields has been found to be generally more accurate than the standard ETSF, but implementation details would make its automation difficult [7,11]. The "In-Cell" capacitance method would also be awkward to automate, in general, because it requires *a priori* knowledge of the slot's capacitance and inductance; however, by assuming the electric field is constant across the aperture, this method basically reduces to the contour approach.

This report describes an automation method for the inclusion of the HTSA and the ETSF into TSAR based on the existence of a "slot data file" that includes the cell indices for where the desired slots are to exist within the FDTD mesh. The principles and techniques of the slot algorithms and the automation design philosophy are presented here. This report does not represent a detailed user's guide to the algorithms. For an HTSA-defined slot, the wall region local to the slot is shorted, and therefore, to change the slot's topology simply requires altering the data file to include the desired cells. For an ETSF-defined slot, the mesh description file must also be modified to include the appropriate slot material in the slot cells. So that the creation of the data file is transparent to the TSAR user, the Lawrence Livermore National Laboratory (LLNL) is modifying the TSAR user interface so that the appropriate data files are generated after the desired slot topology is designed at the solid-model level.

The outline for the report is as follows. In Section 2.1, the theoretical foundations for the HTSA for arbitrary, but planar slot contours is described, along with the essential details for a finite-difference solution. Several results that demonstrate the accuracy of the solution for the deep-slot problem are provided. The ETSF is discussed in Section 2.2 along with an experimental technique to improve its accuracy for planar slots (previous studies have shown that the ETSF adds "apparent" depth to narrow slots [11]). In Section 2.3, the basic form of the data file used to integrate the algorithms into TSAR is described, and the program modules that have been added or changed are noted. Results for a variety of narrow slots are presented in this section, which include: multiple linear slots, rectangular (hatch) apertures, "tee"-shaped slots, and diagonal (zig-zag) apertures, all of which fall on planar walls. A linear aperture that falls on a stair-stepped wall is also presented, and basic limitations of the algorithms are discussed.

It is assumed throughout this paper that the reader has an understanding of the principles and techniques associated with FDTD codes based on the Yee algorithm.

2. ANALYSIS

2.1 *Hybrid Thin-Slot Algorithm (HTSA)*

The HTSA combines an integral-equation formulation for narrow slots in an infinite plane with three-dimensional FDTD codes. This is accomplished by using the FDTD *total* fields local to the slot to define appropriate short-circuit fields that drive the integral equation. Thus, although the integral equation is formally valid for a slot in an infinite plane which radiates into empty "half" spaces, it is only applied in the region that is local to the slot within the FDTD mesh, and therefore, the FDTD code controls the manner in which fields radiate away from the aperture. Because of this, general scatterers may exist in the neighborhood of the slot. The technique is most useful for apertures that are narrow both in width and depth with regard to the FDTD spatial cell.

To develop the HTSA, the transient integral equations for arbitrarily directed slots in a thick, but electrically narrow plane at the highest frequency of interest are derived in Section 2.1.1, and a finite-difference solution technique is provided in Section 2.1.2. Results for a variety of aperture shapes are provided in Section 2.1.3. In Section 2.1.4, the modification required to combine the integral equation with a three-dimensional FDTD code is discussed.

2.1.1 *Transient Integral Equations for Slots in an Infinite, Thick Plane*

A cross section of a deep slot of length, L, depth, d, and width, w, is shown in Fig. 1a. The slot is assumed to be x-directed at this cross section. Both the width and depth are assumed to be electrically narrow at the highest frequency of interest.[3]

[3]In a free-space environment, it has been found that valid frequencies usually satisfy $f < c / [5 \cdot max(d,w)]$ with $L / d >> 1$, $L / w >> 1$.

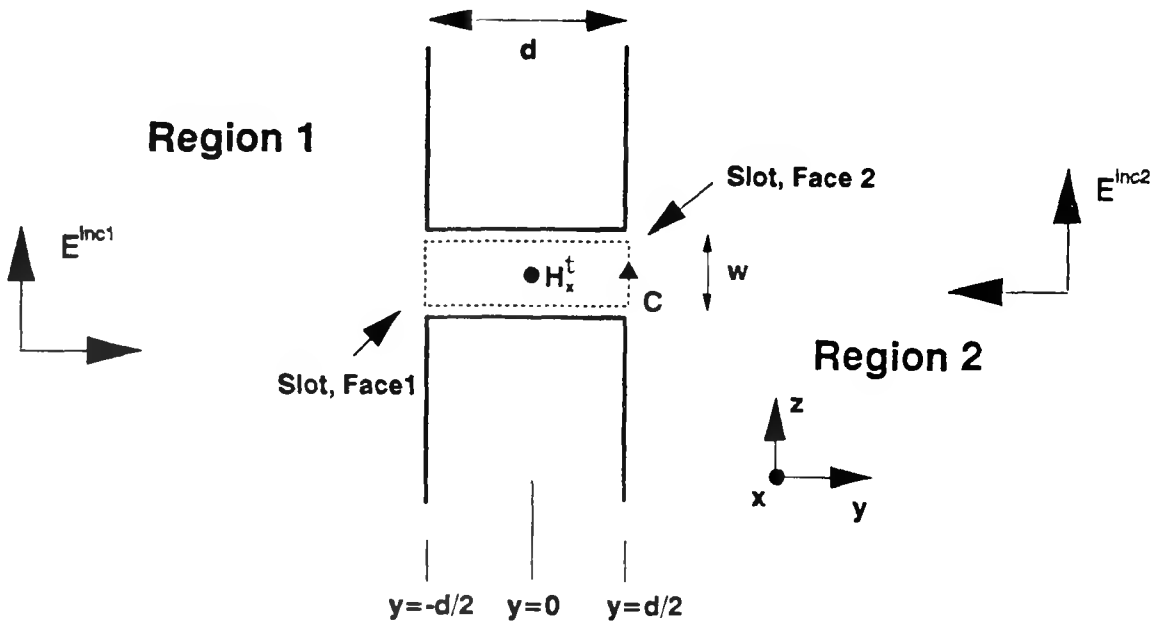

Fig. 1a: x-directed cross section of a deep slot in thick, conducting wall.

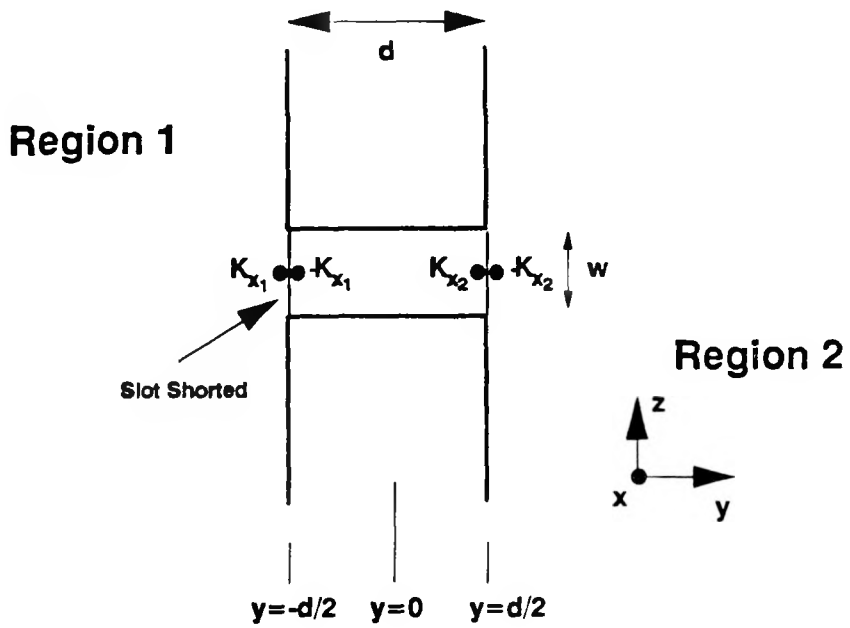

Fig. 1b: Slot shorted and magnetic-current elements added.

When the slot is modeled using the HTSA, the slot is shorted and equivalent magnetic-current elements, K_{x_1} and K_{x_2}, are used to characterize the slot physics (Fig. 1b).

For a general slot in an infinitesimally thin plane, the slot is assumed to be $\hat{s}$ directed as shown in Fig. 2. For the thick-plane problem, Γ is assumed to split into the parallel contours Γ_1 and Γ_2, where Γ_1 falls on the x-z plane at $y = -d/2$ and Γ_2 falls at $y = d/2$. The magnetic currents become K_{s_1}, K_{s_2} on Γ_1, Γ_2, respectively.

For slots in an infinitesimally thin plane, the "dual" problem of arbitrarily directed thin wires in free space has been studied extensively in both the frequency- and time-domains [12–16]. The direct treatment of the general thin-slot problem in an infinitesimally thin plane has received less attention, perhaps because thin-slot results follow readily from the thin-wire equations. A recent detailed treatment of the transient thin-slot problem that provides a good amount of experimental data is by Reed and Butler [17]. An approximate formulation for the transient *deep*-slot problem is presented below. Regions 1 and 2 are assumed to be empty "half" spaces and waves are incident from both regions.

The total magnetic field in Region 1, $\bar{H}^{t1}$, due to the magnetic line source directed along the axis of the slot, $\hat{s}\, K_{s_1}$, is given by

$$\mu_o \frac{\partial}{\partial t} \bar{H}^{t1} = \mu_o \frac{\partial}{\partial t} \bar{H}^{sc1} - \frac{1}{c^2} \frac{\partial^2}{\partial t^2} \int_{\Gamma_1} ds' \, \hat{s}' \, K_{s_1}(s',\tau)\, G(\bar{r},\bar{r}') + \nabla \int_{\Gamma_1} ds' \, \nabla'_{s'} \cdot [\hat{s}' \, K_{s_1}(s',\tau)]\, G(\bar{r},\bar{r}') . \qquad (y \le -d/2) \qquad (1a)$$

In Region 2, the total $\bar{H}$–field becomes

$$\mu_o \frac{\partial}{\partial t} \bar{H}^{t2} = \mu_o \frac{\partial}{\partial t} \bar{H}^{sc2} + \frac{1}{c^2} \frac{\partial^2}{\partial t^2} \int_{\Gamma_2} ds' \, \hat{s}' \, K_{s_2}(s',\tau)\, G(\bar{r},\bar{r}') - \nabla \int_{\Gamma_2} ds' \, \nabla'_{s'} \cdot [\hat{s}' \, K_{s_2}(s',\tau)]\, G(\bar{r},\bar{r}') . \qquad (y \ge d/2) \qquad (1b)$$

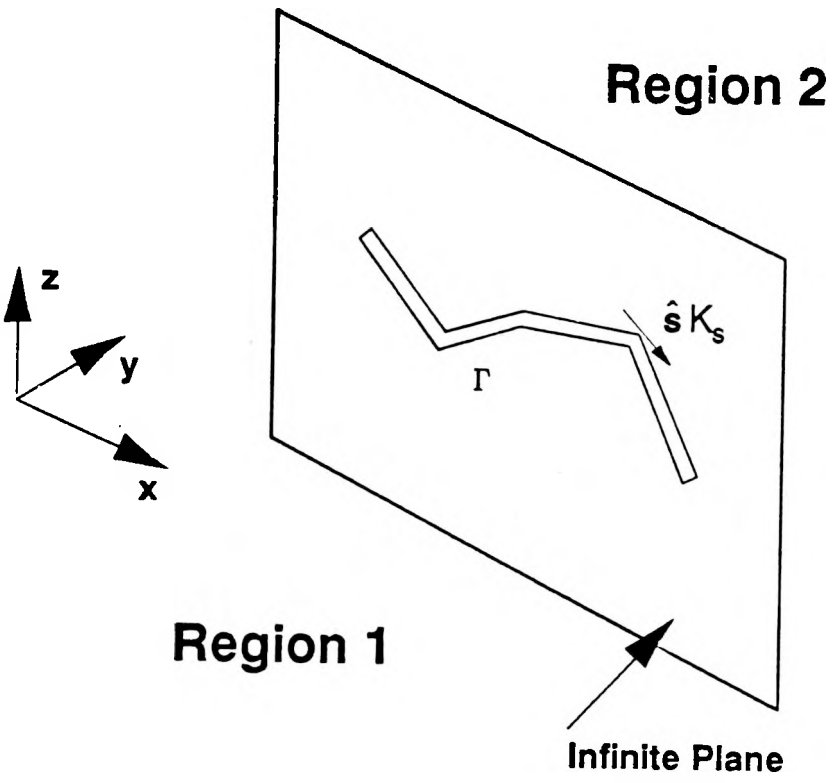

Fig. 2: General slot contour

The retarded time, τ, is $\tau = t - |\bar{r}-\bar{r}'|/c$. It is noted that although two integration contours are used (Γ_1 on Face 1 and Γ_2 on Face 2) these are assumed to be parallel and of equal length. In (1a) and (1b), $\bar{H}^{sc1}$ and $\bar{H}^{sc2}$ represent the $\bar{H}$-fields in Regions 1 and 2, respectively, that would be present with the slot shorted and the magnetic currents absent. $G(\bar{r},\bar{r}') = 1 / [2\pi |\bar{r} - \bar{r}'|]$, but as $\bar{r}$ approaches Γ_1 or Γ_2, $G(\bar{r},\bar{r}')$ is defined to be twice the wire-antenna kernel, given in exact form by,

$$G(\bar{r},\bar{r}') = \frac{1}{4\pi^2}\int_0^{2\pi} d\varphi' \, [\, |\bar{r}-\bar{r}'|^2 + 4\,a^2 \sin^2(\varphi'/2)\,]^{-1/2}, \tag{2a}$$

and in approximate, or thin-wire form by

$$G(\bar{r},\bar{r}') \cong \frac{1}{2\pi}[\, |\bar{r}-\bar{r}'|^2 + a^2\,]^{-1/2}, \tag{2b}$$

where a denotes the equivalent radius.

The problem is to determine K_{s_1} and K_{s_2}. A rigorous formulation would use the appropriate slot-interior Green's function and solve the resulting coupled set of integral equations. Alternatively, for $L/w >> 1$ with both w and d electrically small, an approximate solution that doesn't explicitly require this Green's function has been obtained by following the standard procedure of decomposing the problem into "even" (symmetric) and "odd" (asymmetric) excitations that give rise to $K_{s_1} = (K_{s_1})_{even} + (K_{s_1})_{odd}$, $K_{s_2} = (K_{s_2})_{even} + (K_{s_2})_{odd}$, with $(K_{s_1})_{even} = (K_{s_2})_{even} = K_s$, and $(K_{s_1})_{odd} = -(K_{s_2})_{odd}$. This approach was used in [18,19] and is adopted here.

For the "even" problem, static techniques yield the deep-slot approximate equivalent radius [18]

$$a = (w/4)\, exp[-\pi\, d/(2w)], \tag{3}$$

which assumes a uniform interior electric field.

Because symmetric excitation yields $(K_{s_1})_{even} = (K_{s_2})_{even} = K_s$, the integral equation for solving the "even" problem is basically the same as that for a slot in an infinitesimally thin plane, with the exception that the equivalent radius (3) is used,

$$\frac{1}{2}\mu_o \hat{s} \cdot \frac{\partial}{\partial t} \bar{H}^{sc1} - \frac{1}{2}\mu_o \hat{s} \cdot \frac{\partial}{\partial t} \bar{H}^{sc2} = \frac{1}{c^2}\frac{\partial^2}{\partial t^2}\int_\Gamma ds' \, \hat{s} \cdot \hat{s}' \, K_s(s',\tau)\, G(\bar{r},\bar{r}') -$$

$$\hat{s} \cdot \nabla \int_\Gamma ds' \, \nabla'_{s'} \cdot [\hat{s}' \, K_s(s',\tau)]\, G(\bar{r},\bar{r}'), \qquad (\bar{r} \in \Gamma). \quad (4)$$

Because the slot depth is assumed to be electrically small, the phase variation of the excitation has been neglected between the two faces of the wall.

A non-magnetic slot-gasket contribution is included by adding [19]

$$\frac{1}{2}\frac{d}{w}\left[\mu_o \sigma_g \frac{\partial}{\partial t} K_s(s,t) + \frac{1}{c^2}(\epsilon_g/\epsilon_o - 1)\frac{\partial^2}{\partial t^2} K_s(s,t)\right] \quad (5)$$

to the right-hand side of (4).

The interior $\bar{H}$-field parallel to the magnetic current that results from asymmetric excitation is approximated by the integral form of Faraday's law,

$$\mu_o \frac{\partial}{\partial t}\int_A \bar{H}^t \cdot \hat{s}\, dA = -\oint_C \bar{E}^t \cdot d\bar{\ell}', \quad (6)$$

where the integration contour covers the $\hat{s}$-directed cross section of the slot interior. Assuming the $\bar{H}$-field is constant over the integration area (which is a standard assumption in FDTD codes) and the slot walls are lossless, the interior $\bar{H}$-field directed along the slot is written in terms of the magnetic current as

$$\mu_o \frac{\partial}{\partial t}\int_A \bar{H}^t \cdot \hat{s}\, dA \cong \mu_o\, d\, w\, \hat{s} \cdot \frac{\partial}{\partial t}\bar{H}^t = [K_{s_1} - K_{s_2}] = (K_{s_1})_{odd} - (K_{s_2})_{odd}. \quad (7)$$

Because of the assumption L/w >> 1, an approximation to the H-field can be written in terms of the incident field evaluated at the midpoint of the slot depth [18],

$$(K_{s_1})_{odd} - (K_{s_2})_{odd} \cong \mu_o \, d \, w \, \hat{s} \cdot [\frac{\partial}{\partial t} H^{inc1} + \frac{\partial}{\partial t} H^{inc2}],$$

which implies

$$(K_{s_1})_{odd} \cong \frac{1}{2} \mu_o \, d \, w \, \hat{s} \cdot [\frac{\partial}{\partial t} H^{inc1} + \frac{\partial}{\partial t} H^{inc2}], \tag{8a}$$

$$(K_{s_2})_{odd} \cong -\frac{1}{2} \mu_o \, d \, w \, \hat{s} \cdot [\frac{\partial}{\partial t} H^{inc1} + \frac{\partial}{\partial t} H^{inc2}]. \tag{8b}$$

The total magnetic currents (voltages) at the entering and exiting planes are obtained by adding (8a) or (8b), respectively, to K_s. However, for w/d << 1, L/w >> 1 and L/d >> 1, the gap electric field becomes very uniform through the depth, and therefore, the interior Faraday's law contribution given by (6) is not significant for frequencies which satisfy, in a free-space environment, f < 2 c/L [18,19]. Thus, within this framework, the "even" solution alone can be used effectively for many problems of practical interest.

Considering the x-directed cross section shown in Fig. 1, the total magnetic currents in (1) and the magnetic-current *densities* for Regions 1 and 2, denoted by M_{x_1} and M_{x_2}, are related through the integral $K_{x_{1,2}}(x;t) = \int_{-w/2}^{w/2} dz \, M_{x_{1,2}}(x,z;t)$. Since $\hat{y}$ is assumed to be directed into Region 2, M_{x_1} is related to the transverse electric field in the gap opening, $E^t_{z_1}$, by $\hat{x} \, M_{x_1} = \hat{y} \times (\hat{z} \, E^t_{z_1})$. In Region 2, $\hat{x} \, M_{x_2} = -\hat{y} \times (\hat{z} \, E^t_{z_2})$. Consequently, the average electric field across the gap width is K_{x_1}/w on Face 1 and K_{x_2}/w on Face 2. For the general slot direction, $\hat{s}$, the average electric field across the gap openings become K_{s_1}/w and K_{s_2}/w.

2.1.2 *Finite-Difference Solution*

The finite-difference solution of (4) will be discussed. The numerical solution adopted here is very similar to the method-of-moments solution of the frequency-domain thin-wire equation used in the CHAOS code [12,13] and also in the Mini–NEC code [14]. The solution technique features piecewise-linear (triangle) basis functions with pulse testing. Multiple junctions are accommodated by using overlapping basis functions [12,13]. This procedure has also been applied successfully to the general transient thin–wire equation by Dalke [16], and by Reed and Butler [17] to the transient thin-slot problem. Consequently, only the highlights of the solution procedure, along with some details that are not readily found elsewhere, are presented.

In Fig. 3 is shown a section of a general thin slot that will suffice for defining the basic solution technique. The filled circles are defined as "nodes," the lines connecting the nodes are defined as "segments," and "x" denotes the "segment midpoints." Observe how the triangular basis functions associated with each node cover the structure. Nodes (i=1,2,3...,N) and segment midpoints ($i\pm\frac{1}{2}$) are associated with the following *local* unit vectors in the x-z plane ($\bar{r} = x\,\hat{x} + z\,\hat{z}$):

$$|\bar{s}_i| = [\,(x_{i+\frac{1}{2}} - x_{i-\frac{1}{2}})^2 + (z_{i+\frac{1}{2}} - z_{i-\frac{1}{2}})^2\,]^{1/2}$$

$$|\bar{s}_{i+\frac{1}{2}}| = [\,(x_{i+1} - x_i)^2 + (z_{i+1} - z_i)^2\,]^{1/2}\ ,$$

$$|\bar{s}_{i-\frac{1}{2}}| = [\,(x_i - x_{i-1})^2 + (z_i - z_{i-1})^2\,]^{1/2}\ ,$$

$$\hat{s}_i = [\,(x_{i+\frac{1}{2}} - x_{i-\frac{1}{2}})\,\hat{x} + (z_{i+\frac{1}{2}} - z_{i-\frac{1}{2}})\,\hat{z}\,] \,/\, |\bar{s}_i|\ ,$$

$$\hat{s}_{i+\frac{1}{2}} = [\,(x_{i+1} - x_i)\,\hat{x} + (z_{i+1} - z_i)\,\hat{z}\,] \,/\, |\bar{s}_{i+\frac{1}{2}}|\ ,$$

$$\hat{s}_{i-\frac{1}{2}} = [\,(x_i - x_{i-1})\,\hat{x} + (z_i - z_{i-1})\,\hat{z}\,] \,/\, |\bar{s}_{i-\frac{1}{2}}|\ .$$

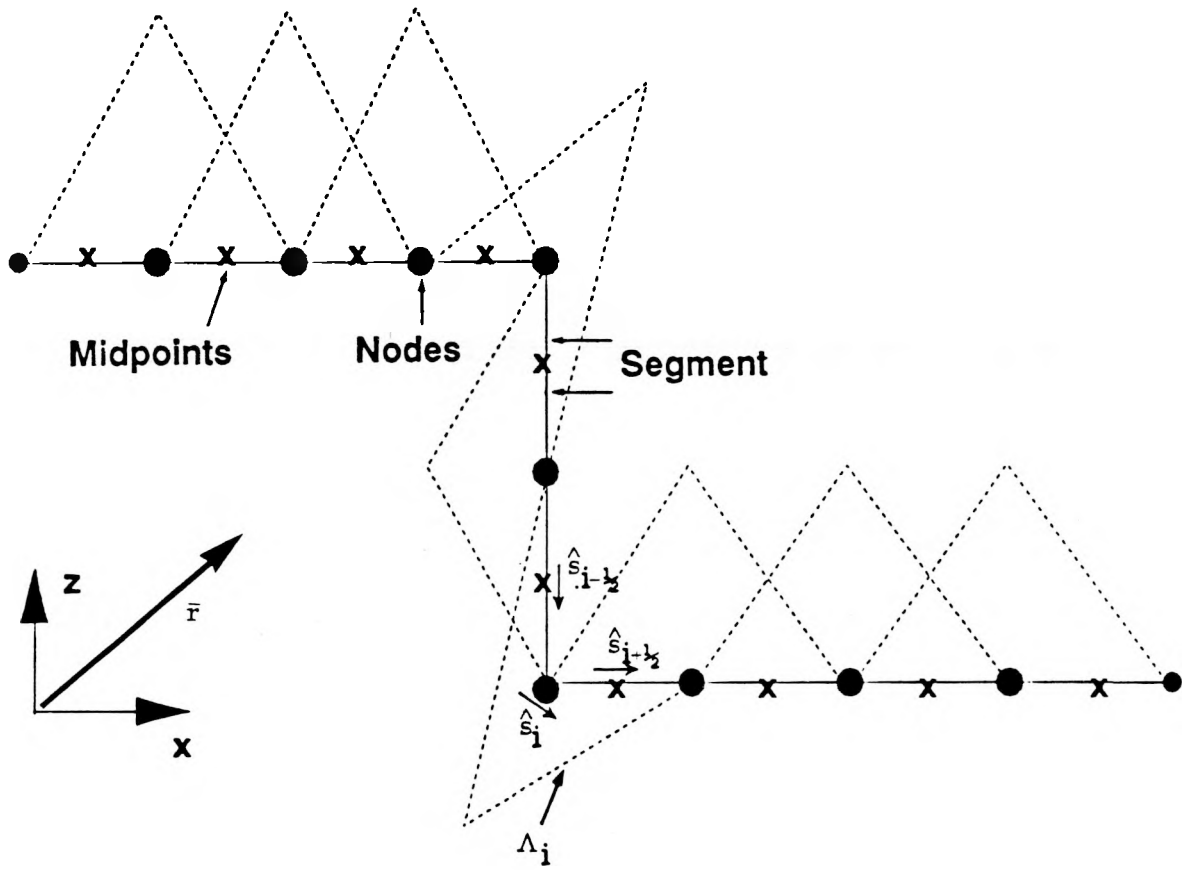

Fig. 3: Section of a slot showing discrete integral-equation solution elements.

The magnetic current is expanded in terms of triangle functions (cf. Fig. 3), $\Lambda_{i'}(s')$, as

$$K_s(s_i,\tau) = \sum_{i'=1}^{N} k_{i'}^{\tau(i,i';n)}\, \Lambda_{i'}(s')\,, \tag{9}$$

where $k_{i'}^{\tau(i,i';n)}$ denote coefficients to be determined and $\tau(i,i';n) = n - int\,[|\bar{r}_i - \bar{r}_{i'}|\,/\,(c\Delta t_s)]$, $t = n\,\Delta t_s$, $n=1,2,...$ ("*int*" denotes "the integer part of").

By using the defined vectors, representing $\hat{s}\cdot\nabla = \partial/\partial s$ as a central difference approximation that is centered at s_i, and using the magnetic-current expansion, the right-hand side of (4) becomes

$$\frac{1}{c^2}\frac{\partial^2}{\partial t^2}\sum_{i'=1}^{N} k_{i'}^{\tau(i,i';n)}\, F_1(i,i') - \frac{1}{|\bar{s}_i|}\sum_{i'=1}^{N} F_2(i,i';n), \tag{10}$$

where

$$F_1(i,i') = \hat{s}_i \cdot \left[\hat{s}_{i'-\frac{1}{2}} \int_{s_{i'-1}}^{s_{i'}} ds'\ \Lambda_{i'}(s')\, G(s_i,s') + \hat{s}_{i'+\frac{1}{2}} \int_{s_{i'}}^{s_{i'+1}} ds'\ \Lambda_{i'}(s')\, G(s_i,s') \right],$$

$$\begin{aligned} F_2(i,i';n) = {} & \frac{1}{|\bar{s}_{i'-\frac{1}{2}}|}\, k_{i'}^{\tau(i+\frac{1}{2},i'-\frac{1}{2};n)} \int_{s_{i'-1}}^{s_{i'}} ds'\ G(s_{i+\frac{1}{2}},s') - \\ & \frac{1}{|\bar{s}_{i'-\frac{1}{2}}|}\, k_{i'}^{\tau(i-\frac{1}{2},i'-\frac{1}{2};n)} \int_{s_{i'-1}}^{s_{i'}} ds'\ G(s_{i-\frac{1}{2}},s') - \\ & \frac{1}{|\bar{s}_{i'+\frac{1}{2}}|}\, k_{i'}^{\tau(i+\frac{1}{2},i'+\frac{1}{2};n)} \int_{s_{i'}}^{s_{i'+1}} ds'\ G(s_{i+\frac{1}{2}},s') + \\ & \frac{1}{|\bar{s}_{i'+\frac{1}{2}}|}\, k_{i'}^{\tau(i-\frac{1}{2},i'+\frac{1}{2};n)} \int_{s_{i'}}^{s_{i'+1}} ds'\ G(s_{i-\frac{1}{2}},s')\,. \end{aligned}$$

Representing the time-derivative in (10) by central differences, and then solving the discretized form of (4) for the magnetic current at the latest time yields the following explicit (time-marching) difference scheme[4]

$$F_1(i,i)\ k_i^{n+1} = \frac{1}{2}\mu_o (c\Delta t_s)^2 \left[\hat{s}_i \cdot \frac{\partial}{\partial t} \bar{H}^{sc1} - \hat{s}_i \cdot \frac{\partial}{\partial t} \bar{H}^{sc2} \right]$$

$$- \sum_{\substack{i'=1 \\ i' \neq i}}^{N} F_1(i,i') \left[k_{i'}^{n-1-int[|\bar{r}_i - \bar{r}_{i'}|/(c\Delta t_s)]} - 2\, k_{i'}^{n-int[|\bar{r}_i - \bar{r}_{i'}|/(c\Delta t_s)]} \right]$$

$$- \sum_{\substack{i'=1 \\ i \neq i'}}^{N} F_1(i,i')\ k_{i'}^{n+1-int[|\bar{r}_i - \bar{r}_{i'}|/(c\Delta t_s)]} + \frac{(c\Delta t_s)^2}{|\bar{s}_i|} \sum_{i'=1}^{N} F_2(i,i';n) \ ,$$

$$i=1,2,3,..,N; \quad n=1,2... \qquad (11)$$

To simplify the evaluation of F_1, the standard approximation,

$$F_1(i,i') = \hat{s}_i \cdot \left[\hat{s}_{i'-\frac{1}{2}} \int_{s_{i'-\frac{1}{2}}}^{s_{i'}} ds'\ G(s_i,s') + \hat{s}_{i'+\frac{1}{2}} \int_{s_{i'}}^{s_{i'+\frac{1}{2}}} ds'\ G(s_i,s') \right]$$

may be used effectively, which is simply a statement that triangles over a full interval can be replaced by pulses over a half interval when the spacing between nodes is electrically small.

For $i \neq i'$, the thin-wire kernel (2b) is used for $G(s_i,s')$, which integrates to the following concise forms:

---

[4]It is important to note that when overlaping basis functions are used to model a junction with three or more slots, Eq. (11) becomes a matrix problem because several basis functions are now centered at the same spatial position.

$$\int_{s_{i'-1}}^{s_{i'}} ds'\ G(s_{i\pm\frac{1}{2}},s') =$$

$$\frac{1}{2\pi}\ ln\left[\frac{(\bar{r}_{i'} - \bar{r}_{i\pm\frac{1}{2}})\cdot\hat{s}_{i'-\frac{1}{2}} + [\ a^2 + |\bar{r}_{i'} - \bar{r}_{i\pm\frac{1}{2}}|^2\ ]^{1/2}}{(\bar{r}_{i'-1} - \bar{r}_{i\pm\frac{1}{2}})\cdot\hat{s}_{i'-\frac{1}{2}} + [\ a^2 + |\bar{r}_{i'-1} - \bar{r}_{i\pm\frac{1}{2}}|^2\ ]^{1/2}}\right],$$

$$\int_{s_{i'}}^{s_{i'+1}} ds'\ G(s_{i\pm\frac{1}{2}},s') =$$

$$\frac{1}{2\pi}\ ln\left[\frac{(\bar{r}_{i'+1} - \bar{r}_{i\pm\frac{1}{2}})\cdot\hat{s}_{i'+\frac{1}{2}} + [\ a^2 + |\bar{r}_{i'+1} - \bar{r}_{i\pm\frac{1}{2}}|^2\ ]^{1/2}}{(\bar{r}_{i'} - \bar{r}_{i\pm\frac{1}{2}})\cdot\hat{s}_{i'+\frac{1}{2}} + [\ a^2 + |\bar{r}_{i'} - \bar{r}_{i\pm\frac{1}{2}}|^2\ ]^{1/2}}\right].$$

For $i = i'$, only the integrals in the F_1 function are of interest, and the exact-kernel (2a) should be used for slots that are not purely linear to help avoid instability in a numerical solution, as well as improve accuracy:

$$\int_{s_i}^{s_{i+\frac{1}{2}}} ds'\ G(s_i,s') = \frac{1}{4\pi^2}\int_0^{\frac{1}{2}|\bar{s}_{i+\frac{1}{2}}|} du \int_0^{2\pi} d\varphi' \frac{1}{[\ u^2 + 4\ a^2\ sin^2(\varphi'/2)\ ]^{1/2}}.$$

By interchanging the integration order, it is straightforward to simplify the right side to

$$\frac{1}{\pi^2}\int_0^{\pi/2} d\xi\ \ ln\left[\ 1 + [\ 1 + (\frac{4\ a}{|\bar{s}_{i+\frac{1}{2}}|})^2\ sin^2(2\ \xi)\ ]^{1/2}\right] - \frac{1}{2\pi}\ ln(\frac{2\ a}{|\bar{s}_{i+\frac{1}{2}}|}).$$

Similarly,

$$\int_{s_{i-\frac{1}{2}}}^{s_i} ds'\ G(s_i,s') =$$

$$\frac{1}{\pi^2}\int_0^{\pi/2} d\xi\ ln\left[1+\left[1+\left(\frac{4\ a}{|\bar{s}_{i-\frac{1}{2}}|}\right)^2 sin^2(2\ \xi)\right]^{1/2}\right] - \frac{1}{2\ \pi}\ ln\left(\frac{2\ a}{|\bar{s}_{i-\frac{1}{2}}|}\right).$$

The integrals over the *ln* function are easily evaluated numerically. Note that for 4 a / $|\bar{s}_{i\pm\frac{1}{2}}| << 1$, the integrals over the exact kernel become simply $ln\,[|\bar{s}_{i\pm\frac{1}{2}}|/a]/(2\ \pi)$.

2.1.3 *Results for Several Slot Configurations*

In Fig. 4 is shown a deep, linear slot. Figures 5 through 8 compare results for the spectrum of the electric field in the entering and exiting planes (Face 1 and Face 2, respectively) of a 1-cm-deep slot as obtained using Eq. (4) and the "odd" contributions (8a) and (8b), and a method-of-moments (MoM) solution that fully solves the coupled integral equations appropriate for a deep slot [20]. The results correspond to unit amplitude plane-wave excitation. The agreement is generally very good up to the point where the electrical depth of 1 cm becomes significant (5 to 6 GHz, which is where a full gridded FDTD solution will generally fail when using a 1-cm spatial cell).

These results demonstrate that the integral-equation solution with the appropriate equivalent radius adequately solves slots with significant depth. Observe that for w/d << 1, L/w >> 1 and L/d >> 1, the variation between the voltages on the two faces decreases significantly for frequencies that satisfy f < 2 c/L, and therefore the "even" solution given by (4) suffices (cf. Figs. 7 and 8).

Figure 9 depicts some complex aperture shapes that include: 1) A hatch; 2) A tee; and 3) A zig–zag (diagonal slot). The slot depth is set to zero (d=0). Input impedance results obtained using Eq. (4) without the "odd" contributions (8a) and

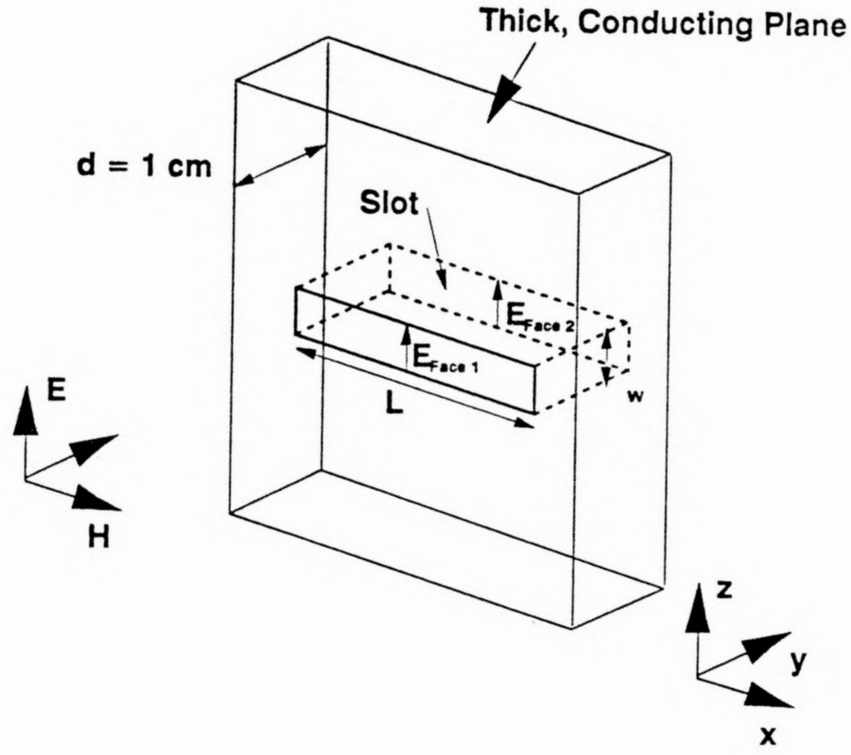

Fig. 4: Deep slot used for verifying transient integral equations.

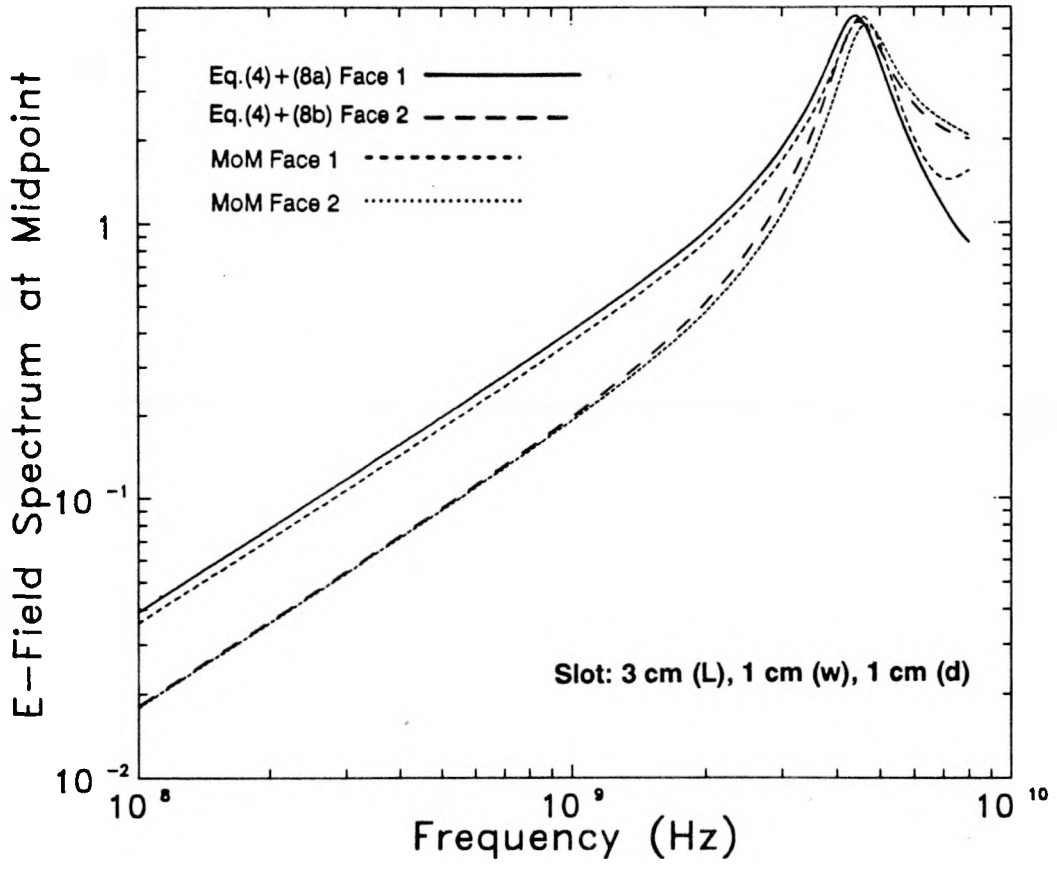

Fig. 5: Gap electric field results for L = 3 cm, w = 1 cm and d = 1 cm. The magnitude of the spectrum of electric field is shown based on Eq. (4) with (8a) and (8b), and coupled MoM solution.

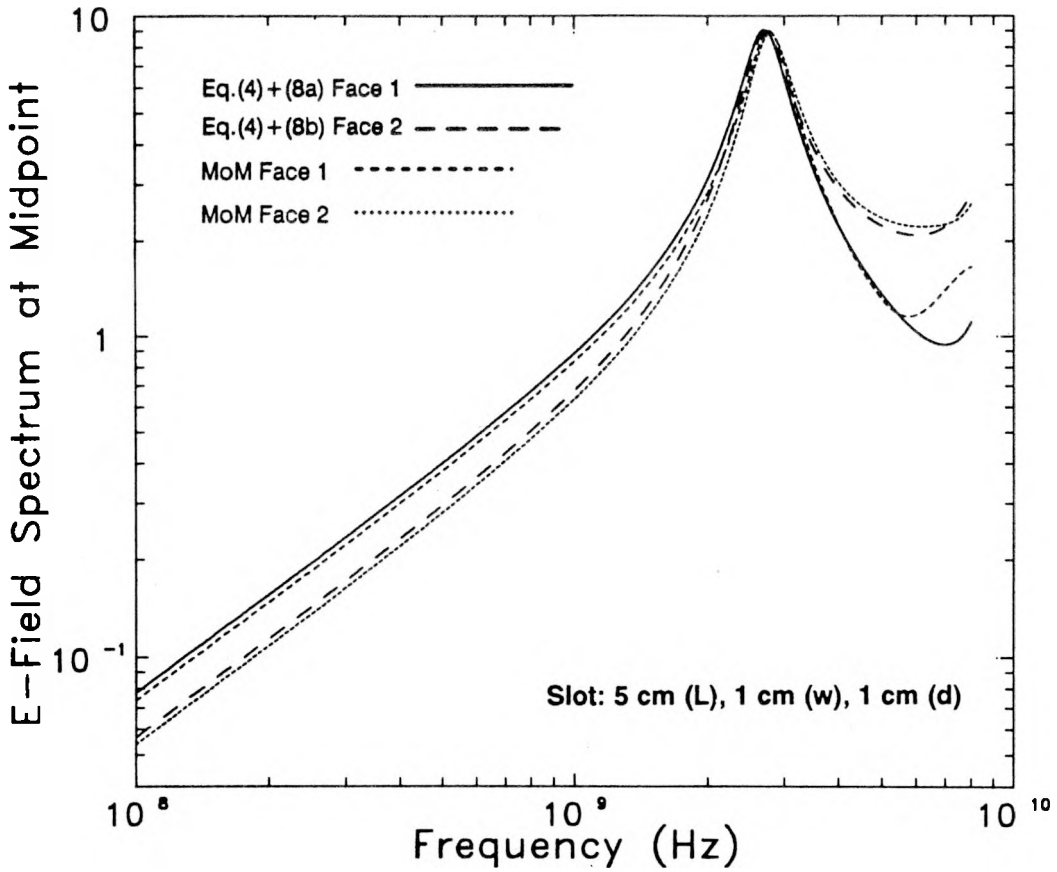

Fig. 6: Gap electric field results for L = 5 cm, w = 1 cm and d = 1 cm. The magnitude of the spectrum of electric field is shown based on Eq. (4) with (8a) and (8b), and coupled MoM solution.

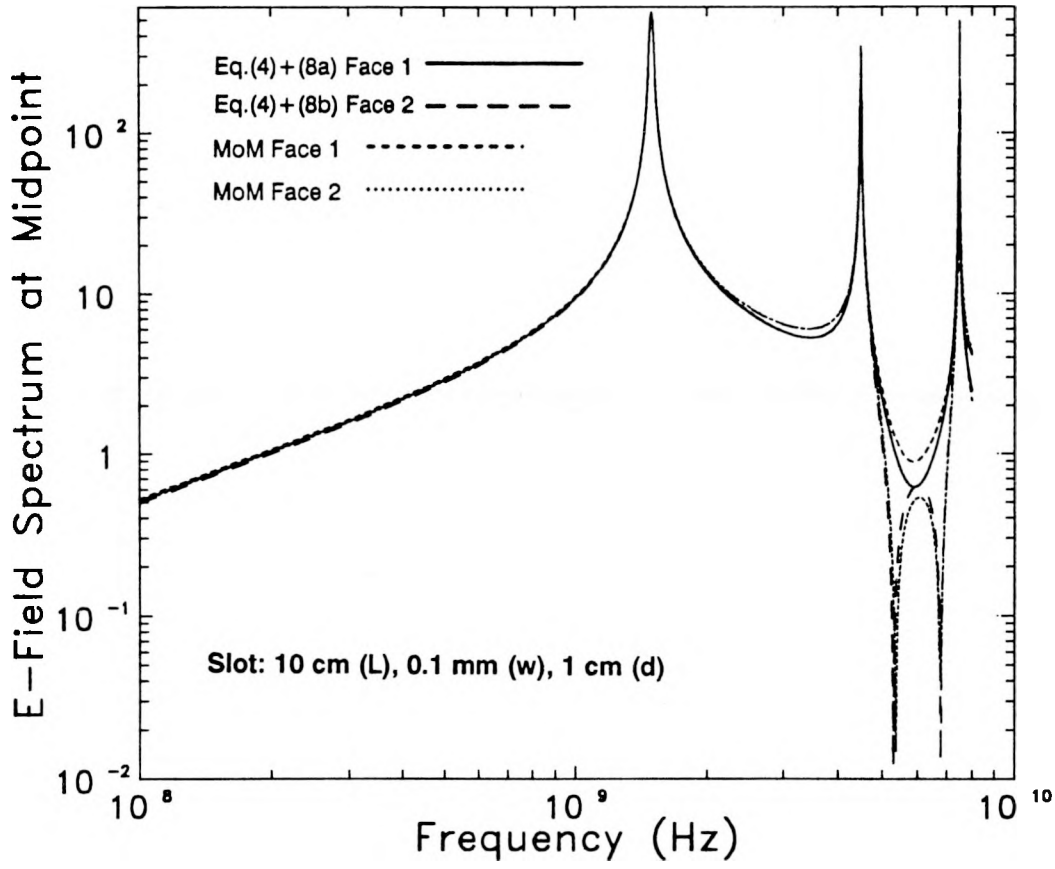

Fig. 7: Gap electric field results for L = 10 cm, w = 0.1 mm and d = 1 cm. The magnitude of the spectrum of electric field is shown based on Eqs. (4) with (8a) and (8b), and coupled MoM solution.

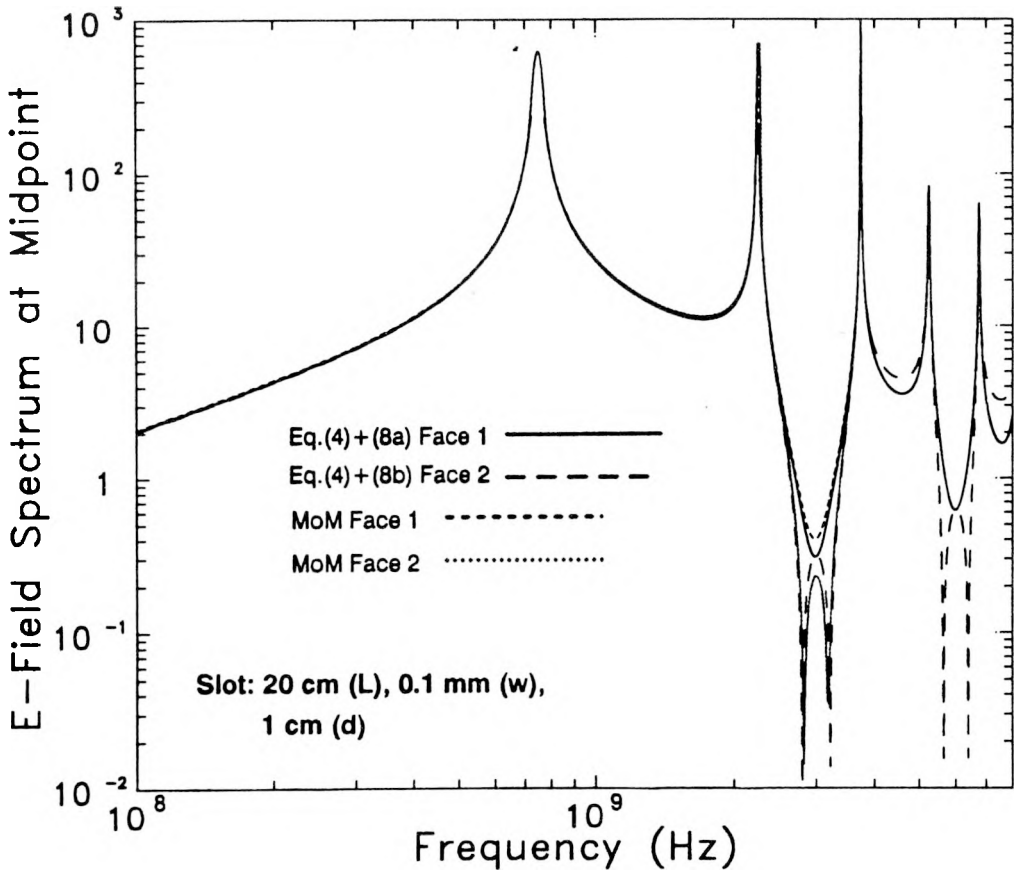

Fig. 8: Gap electric field results for L = 20 cm, w = 0.1 mm and d = 1 cm. The magnitude of the spectrum of electric field is shown based on Eqs. (4) with (8a) and (8b), and coupled MoM solution.

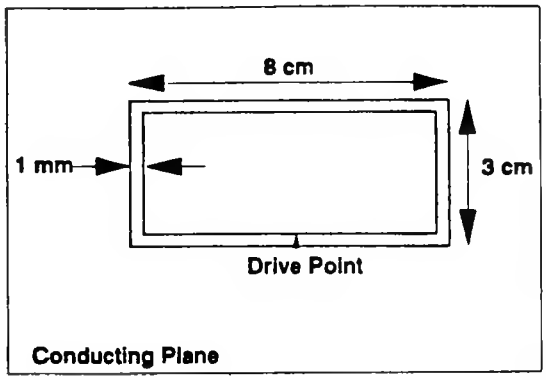

(a)

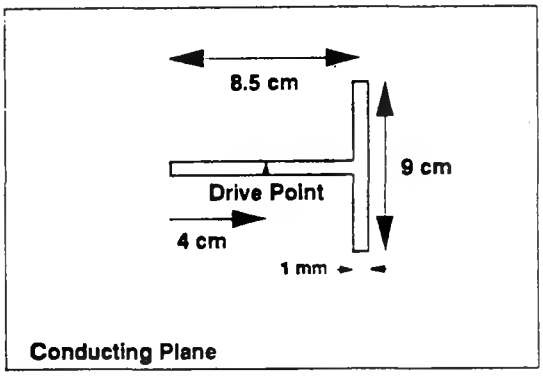

(b)

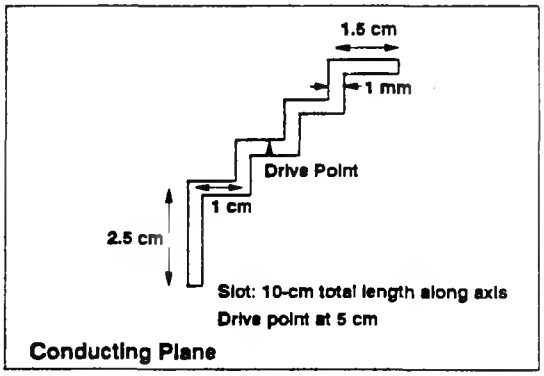

(c)

Fig. 9: (a) Hatch aperture; (b) Tee aperture ; (c) Zig-Zag (Diagonal) aperture.

(8b) are provided in Figure 10 along with similar results obtained using the frequency-dependent thin-wire-code GEMACS [21] (recall that the slot input impedance, $Z_{in_{slot}}$, is related to the wire input impedance, $Z_{in_{wire}}$, by $Z_{in_{slot}} = (\eta_0/2)^2 / Z_{in_{wire}}$).

2.1.3.1 *Convergence Considerations*

Convergence of the integral-equation solution has been found to be a minor problem when bends exist. For low- to medium-resolution solutions (20 to 40 basis functions, or nodes, per wavelength), predicted resonances are about 3 percent *above* the "correct" frequency. To reduce the error to less than one percent usually requires 80 or more nodes per wavelength, which can induce excessive computational and memory overhead. It has been found that by increasing the length of open-end geometries by 1 to 2 percent, high-resolution accuracy is obtained with a low– to medium-resolution solution, as shown in Fig. 11 for the zig-zag slot of Fig. 9c. This length-increase solution has been observed with the straight slot [13]. Unfortunately, the precise length correction varies with the topology of the slot (obviously, the length is not well defined for slots with multiple junctions). *For slots with right-angle bends, one-quarter of the slot's maximum spatial delta is appended to each open end such that the sum over all slot segments is not increased by more than* 2½ %.

2.1.4 *Theoretical Foundations to Integrate Integral-Equation Formulation into TSAR*

The HTSA was introduced in [11], and the basic technique has been further studied in [17,22,23]. The reader is referred to these references for additional information beyond what is presented here.

In Fig. 12 is shown a thick wall modeled on tangential $\mathbf{E}$-fields using a typical FDTD mesh. When the HTSA is used, the slot is shorted and its physics is described

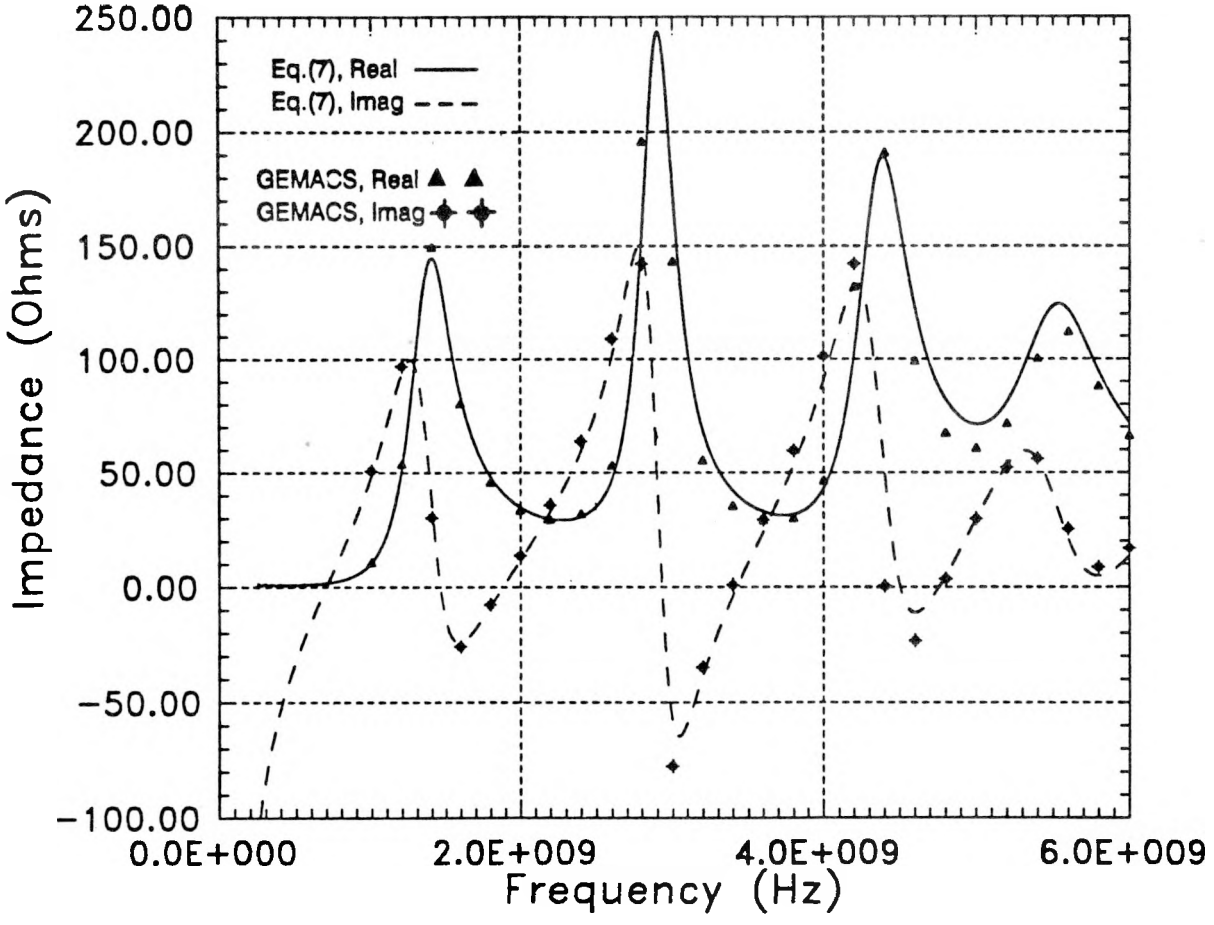

Fig. 10a: Hatch input impedance. Basis functions: Eq.(7), 88, GEMACS, 176.

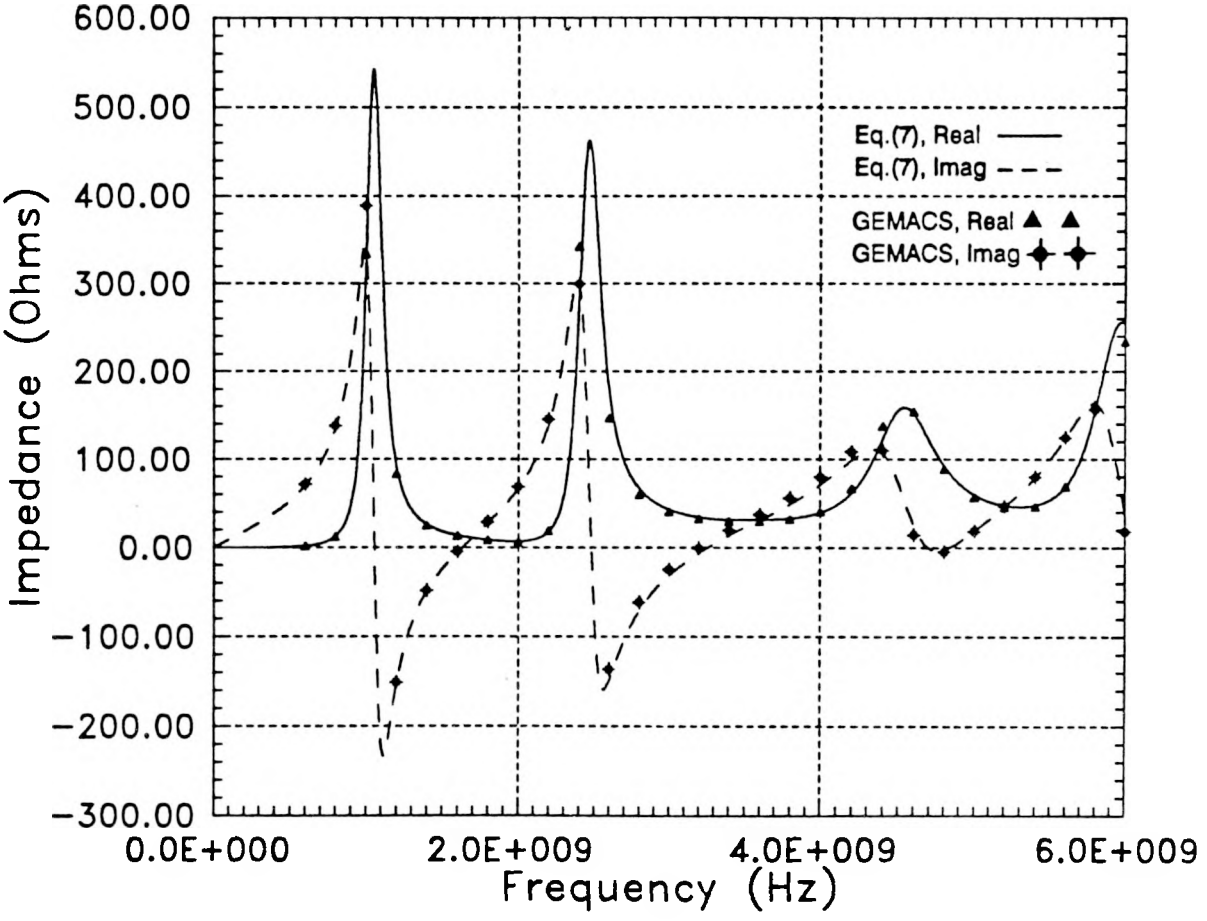

Fig. 10b: Tee input impedance. Basis functions: Eq. (7) 75, GEMACS, 228.

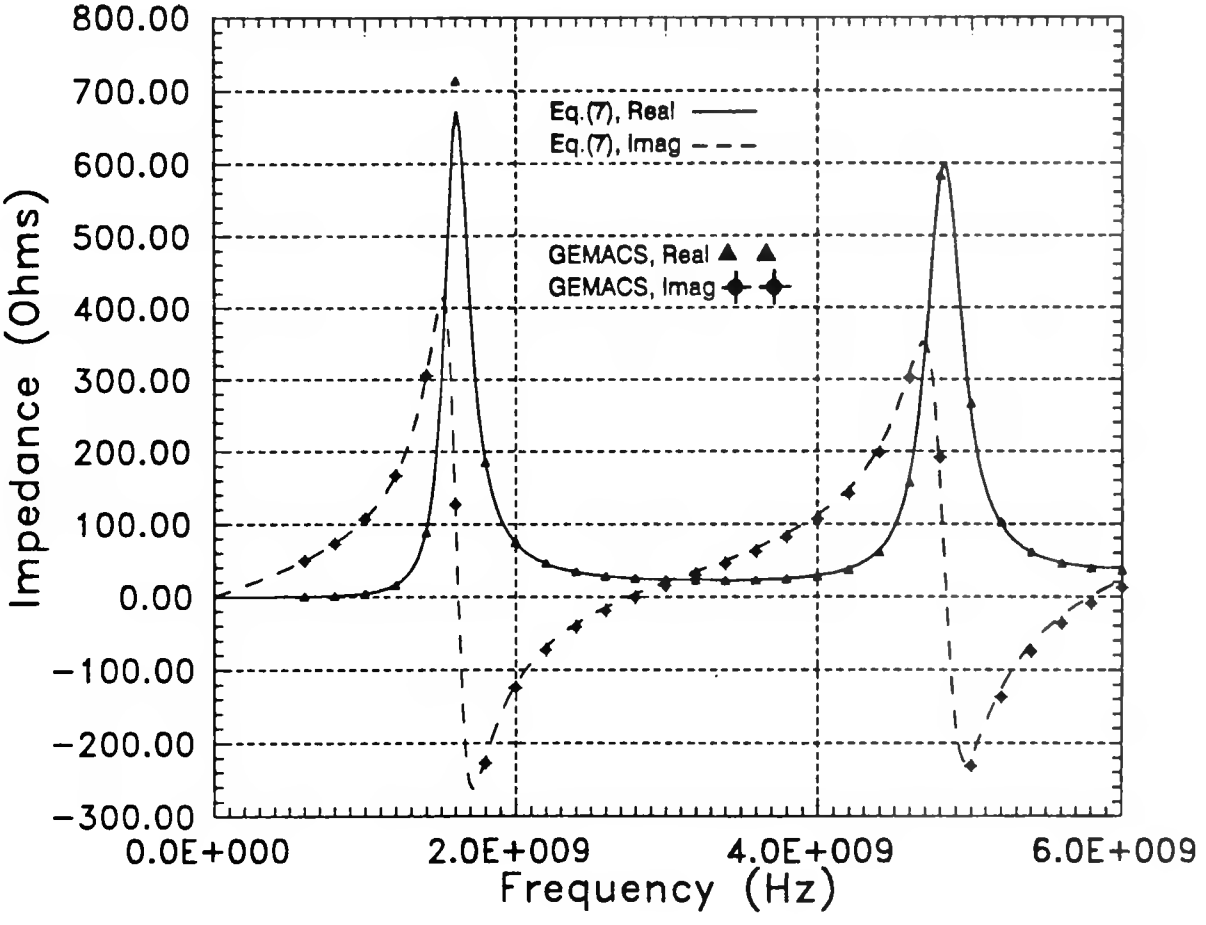

Fig. 10c: Zig-Zag input impedance. Basis functions: Eq. (7) 132, GEMACS, 132.

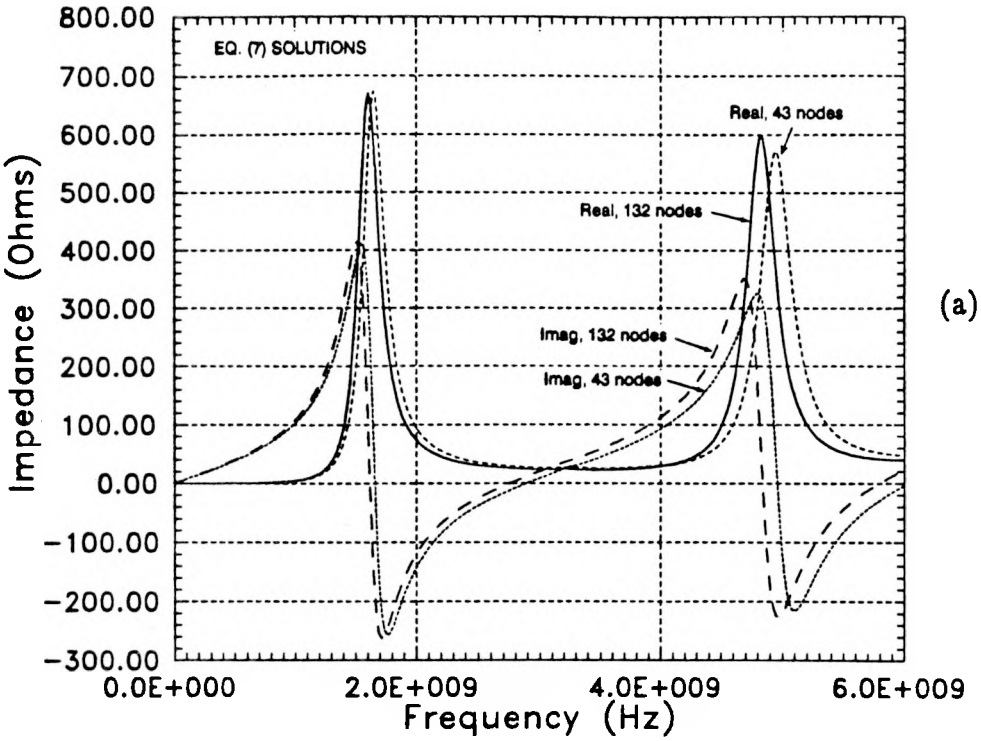

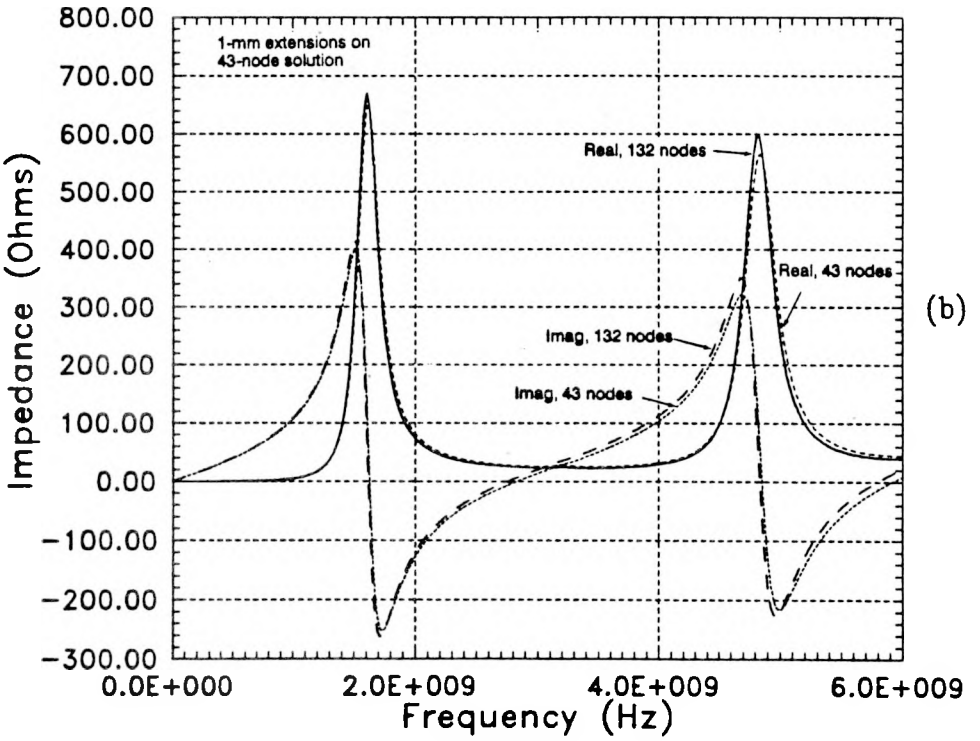

Fig. 11: (a) Zig-Zag input impedance using 132 nodes and 43 nodes; (b) Same number of nodes as (a), but 1 mm is appended to each open end of the slot for the low-resolution solution.

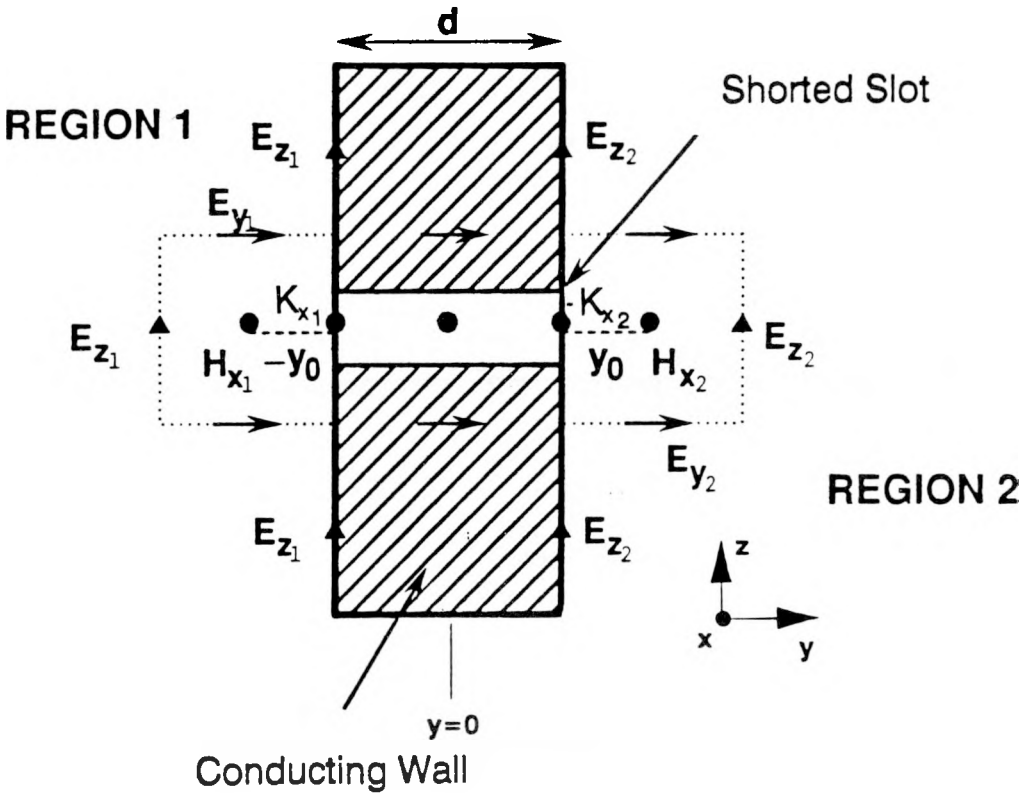

Fig. 12: FDTD wall model based on tangential electric fields.

by the equivalent magnetic-current elements, K_{x_1} and K_{x_2}. The FDTD $\mathbf{H}$-fields local to the slot, denoted as $\mathbf{H}_{x_1}$ and $\mathbf{H}_{x_2}$ in the Fig. 12 cross section, are total fields, and therefore, the "short-circuit" fields required by integral-equation (4), specialized to the x direction, are well approximated by

$$H_x^{sc1} = \mathbf{H}_{x_1} - \mathscr{H}_{x_1} \; ; \quad H_x^{sc2} = \mathbf{H}_{x_2} - \mathscr{H}_{x_2}, \tag{12a}$$

where $\mathscr{H}_{x_2}$ represents the field radiated by K_{x_2} based upon the infinite-plane/empty-half-space expression ($G(\bar{r},\bar{r}') = 1 \,/\, [2\,\pi\,|\bar{r}-\bar{r}'\,|]$)

$$\mu_o \frac{\partial}{\partial t}\mathscr{H}_{x_2} =$$

$$\frac{1}{c^2}\frac{\partial^2}{\partial t^2}\int_{\Gamma_2} dx'\, K_{x_2}(s',\tau)\, G(\bar{r},\bar{r}') - \hat{x}\cdot\nabla\int_{\Gamma_2} dx'\, \nabla'_x\cdot[\hat{x}\, K_{x_2}(s',\tau)]\, G(\bar{r},\bar{r}')\,,$$

$$(y = d/2 + y_o,\ y_o >> a) \tag{12b}$$

with $\mathscr{H}_{x_1}$ similar. Equations (12a) and (12b) are easily generalized for arbitrary slot direction, $\hat{s}$ (cf. Section 2.1.1). By extracting the directly radiated contribution out of the total FDTD field, coupling to the aperture by neighboring obstacles is accounted for in the short-circuit terms.

Although the slot integral equation can accommodate arbitrary slot contours, the magnetic currents that result must be used to drive the FDTD mesh, and therefore, it has been found that they must align with the location that the FDTD code would usually place electric fields. For example, Fig. 13a depicts a linear slot that runs diagonally in the x-z plane. Directly modeling this slot, the slot integral equations would yield magnetic currents that are $\hat{s} = (\hat{x} + \hat{z})/\sqrt{2}$ directed, as shown in Fig. 13b. Standard FDTD codes, however, are forced to model this non-grid aligned slot as the stair-stepped slot shown in Fig. 13c. The electric fields shown in Fig. 13c

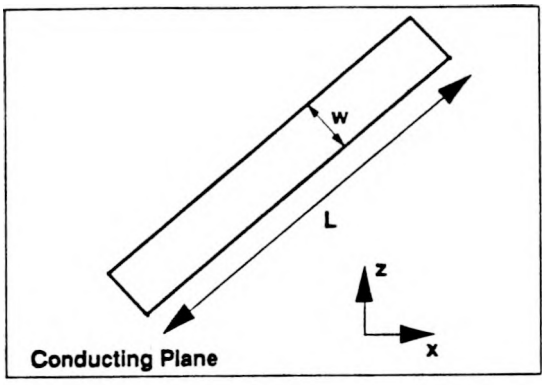

(a)

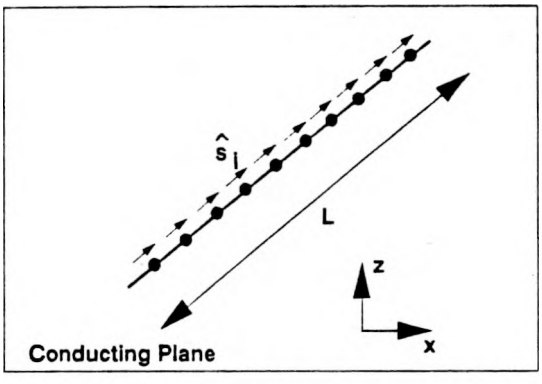

(b)

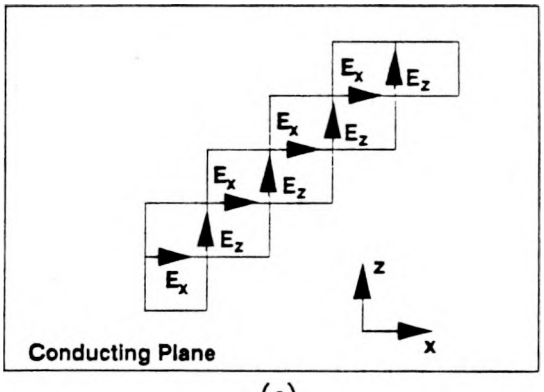

(c)

Fig. 13: Models for a diagonal slot. (a) Actual slot; (b) Possible integral equation model; (c) FDTD model.

"drive" the FDTD mesh away from the slot. To drive the FDTD mesh properly using the HTSA, it has been found that the resulting magnetic currents must, in fact, align with these electric fields, which forces the HTSA diagonal slot to be modeled as a stair case as well. Attempting to drive the FDTD mesh with the HTSA magnetic currents that are truly diagonally directed has not been successful, but further study of this problem is necessary.

Forcing alignment with the FDTD mesh, the magnetic currents are strictly x, y, or z directed depending upon the location of the slot in three-dimensional space and the node position along the slot's axis. The magnetic currents from the integral-equation solution are subsequently appended to the discrete **H**-field Maxwell's equations (FDTD Yee cell assumed, and henceforth suppressing the additional subscripts 1 or 2 on the FDTD fields),

$$\mathbf{H}_x^{n+1}(i,j,k) = \mathbf{H}_x^{n}(i,j,k) + \frac{\Delta t}{\mu_o}\left[\frac{\mathbf{E}_y^{n}(i,j,k+1) - \mathbf{E}_y^{n}(i,j,k)}{\Delta_z}\right] - \frac{\Delta t}{\mu_o}\left[\frac{\mathbf{E}_z^{n}(i,j+1,k) - \mathbf{E}_z^{n}(i,j,k)}{\Delta_y}\right] \pm \frac{\Delta t}{\mu_o}\frac{1}{\Delta_z\,\Delta_y} K_{x_{1,2}}^{n},$$

$$\mathbf{H}_y^{n+1}(i,j,k) = \mathbf{H}_y^{n}(i,j,k) + \frac{\Delta t}{\mu_o}\left[\frac{\mathbf{E}_z^{n}(i+1,j,k) - \mathbf{E}_z^{n}(i,j,k)}{\Delta_x}\right] - \frac{\Delta t}{\mu_o}\left[\frac{\mathbf{E}_x^{n}(i,j,k+1) - \mathbf{E}_x^{n}(i,j,k)}{\Delta_z}\right] \pm \frac{\Delta t}{\mu_o}\frac{1}{\Delta_z\,\Delta_x} K_{y_{1,2}}^{n},$$

$$\mathbf{H}_z^{n+1}(i,j,k) = \mathbf{H}_z^{n}(i,j,k) + \frac{\Delta t}{\mu_o}\left[\frac{\mathbf{E}_x^{n}(i,j+1,k) - \mathbf{E}_x^{n}(i,j,k)}{\Delta_y}\right] - \frac{\Delta t}{\mu_o}\left[\frac{\mathbf{E}_y^{n}(i+1,j,k) - \mathbf{E}_y^{n}(i,j,k)}{\Delta_x}\right] \pm \frac{\Delta t}{\mu_o}\frac{1}{\Delta_x\,\Delta_y} K_{z_{1,2}}^{n},$$

where the usual FDTD spatial indices i ,j ,k correspond to movement along x, y, z, respectively, n denotes a generic time index, but observe that the **E** and **H** fields are separated in time by $\Delta t/2$, and the minus sign is used for the magnetic currents

radiating into Region 1, while the plus sign is for Region 2. Observe that the wall is shorted when the HTSA is used, and therefore, the tangential electric fields are zero.

The HTSA is summarized as follows. At each time step, the slot magnetic current is obtained using the short-circuit fields based on the *total* FDTD $\mathbf{H}$-fields local to the slot with the directly radiated field removed as described by (12a) and (12b) (or a similar equation appropriate for different components). The magnetic current is then appended to the appropriate FDTD equation local to the slot, where the slot has been shorted within the FDTD mesh. Each time step proceeds in this manner.

Using Eq. (4) with the "odd" voltage modifications (8a) and (8b) represent the preferred approach for the HTSA; however, including the "odd" contributions introduces implementation complications because the directly radiated field that is subtracted from the FDTD total field must be altered in a non-trivial way for each region. The most efficient approach is to use only the "even" solution obtained directly from Eq. (4). This was found to be successful for the linear slots studied in [11], and is the equation upon which the HTSA is based here; thus, $K_{s_1}=K_{s_2}=K_s$. This decision is based upon the fact that the HTSA is most appropriately used for the case that *both* the slot width and depth are narrow compared to the FDTD spatial cell. However, as shown in Section 2.3, the HTSA does, in fact, work very well for slot depths that are equal to an FDTD spatial cell size of 1 cm, which would correspond to a fairly thick wall in practice.

An interesting technical feature of the HTSA is that both the spatial step and the time step used in the discrete integral-equation solution can be chosen to be much smaller than the corresponding values used in the FDTD code without introducing stability problems. Because of this, the HTSA can yield very high-resolution solutions for the slot physics.

2.2 *Direct FDTD Contour Methods to Model Narrow Slots*

The finite-difference equations used in standard FDTD codes can be derived directly from the integral form of Faraday's and Ampere's laws [7]. By applying Faraday's law to contour C in Fig. 14 that contains a narrow slot of width w, the following modified FDTD equation is obtained when the electric field is assumed constant across the aperture:

$$\mathbf{H}_x^{n+1}(i,j,k) = \mathbf{H}_x^{n}(i,j,k) + \frac{\Delta t}{\mu_o}\left[\frac{\mathbf{E}_y^{n}(i,j,k+1) - \mathbf{E}_y^{n}(i,j,k)}{\Delta_z}\right] - \frac{\Delta t}{\mu_o}\frac{1}{\Delta_y}\left[\mathbf{E}_z^{n}(i,j+1,k) - \left(\frac{w}{\Delta_z}\right)\mathbf{E}_z^{n}(i,j,k)\right]. \tag{13}$$

For general slot orientation, other components follow similarly. The principal modification introduced by the contour method is the (w/Δ_z) term that multiplies $\mathbf{E}_z^n(i,j,k)$. It is noted that for $\mathbf{H}_x$ *inside* the slot depth, no modifications to the standard FDTD equation are required [7,8].

Equation 13 is an appropriate modification for the case that conducting walls are defined on tangential $\mathbf{E}$ fields and has been denoted an "E-wall thin-slot formalism," or ETSF [11]. Additional modifications to the Faraday's law contour can be made so that it is possible to define walls on tangential $\mathbf{H}$ fields [7], and this method has been denoted an "H-wall thin-slot formalism," or HTSF [11]. Although a general implementation of the HTSF is awkward because the contours associated with an entire wall must be modified as well as those local to the aperture, this method has been shown to be the preferred *contour* method for modeling narrow slots [11]. This is because the standard ETSF tends to model the slot as being one FDTD cell deeper than the actual depth anticipated [11], which is a problem that does not occur with the HTSF.

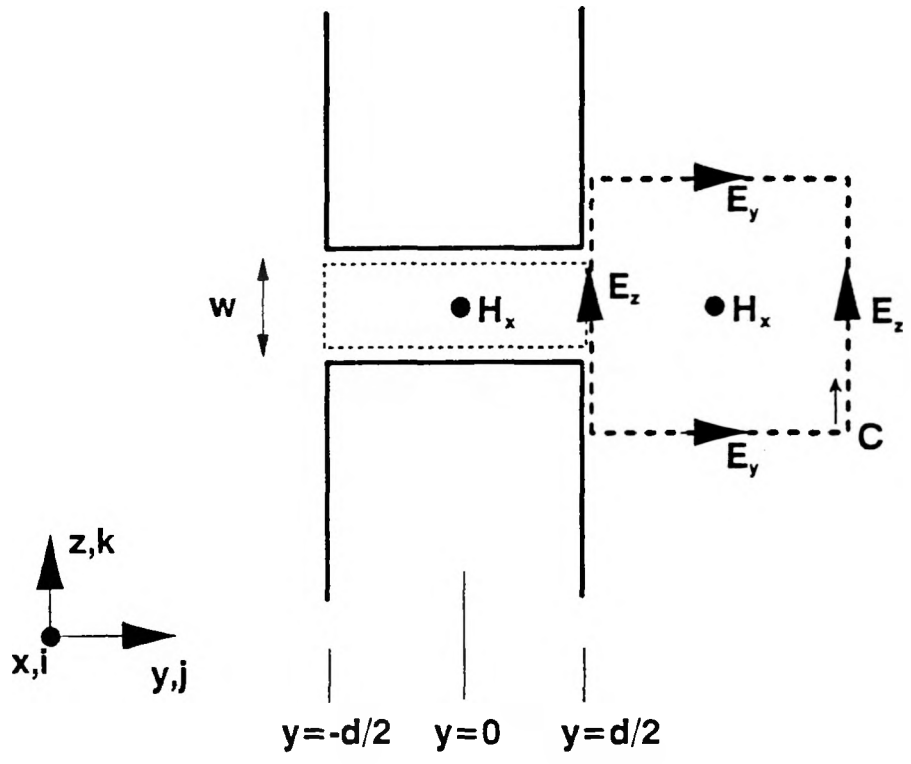

Fig. 14: Faraday's law contour to generate modified FDTD equation local to the aperture.

The standard ETSF applies Eq. (13), or a similar equation that depends upon the appropriate field component involved, to the entering and exiting planes of the slot. The apparent one-cell depth increase noted above results because the FDTD Ampere's law equation for the gap field inherently assumes that the electric field is an average over one cell that extends one-half cell *outside* the slot to one-half cell inside. It has been found through numerical experiments that this depth error can often be reduced by simply reducing the slot depth by one cell. For example, Fig. 15a shows a narrow slot that is two cells deep along with the apparent depth increase that results by the traditional ETSF. Reducing the slot depth by one cell and applying the ETSF equation at this shifted interface simulates the slot shown in Fig. 15b. Shifting the slot on the entering plane instead of the exiting plane simulates the slot shown in Fig. 15c. Note that the simulated slot depth is the proper wall thickness with the shifted cases.

A tee shaped slot with a width of 1 mm, and a depth of 1 cm (1 FDTD cell) that couples into a rectangular cavity is shown in Fig. 16a. Results for an interior E_z are shown in Fig. 16b. The results are based on an HTSF model (very accurate), the standard ETSF, and the shifted ETSF as described above. The standard ETSF results correspond to a 2-cm-deep slot (2 FDTD cells). It is seen that the shifted ETSF yields results that agree very well with the HTSF, at the interior point selected, independent of whether the shift was applied on the entering or exiting slot planes. However, for other choices of interior points the agreement has been found to be not as good, which could be related to the apparent theoretical difficulty that the inner aperture in Fig. 15c should be overdriven due to the neighboring 1-cell-wide slot that has been introduced.

The shifted ETSF may prove to be a useful alternative method, but at this time the *standard* ETSF has been defined to be the default contour method in TSAR. Although the standard ETSF can lead to amplitude errors as large as a factor of two too small for one-cell deep slots that are very narrow, it is most appropriately used

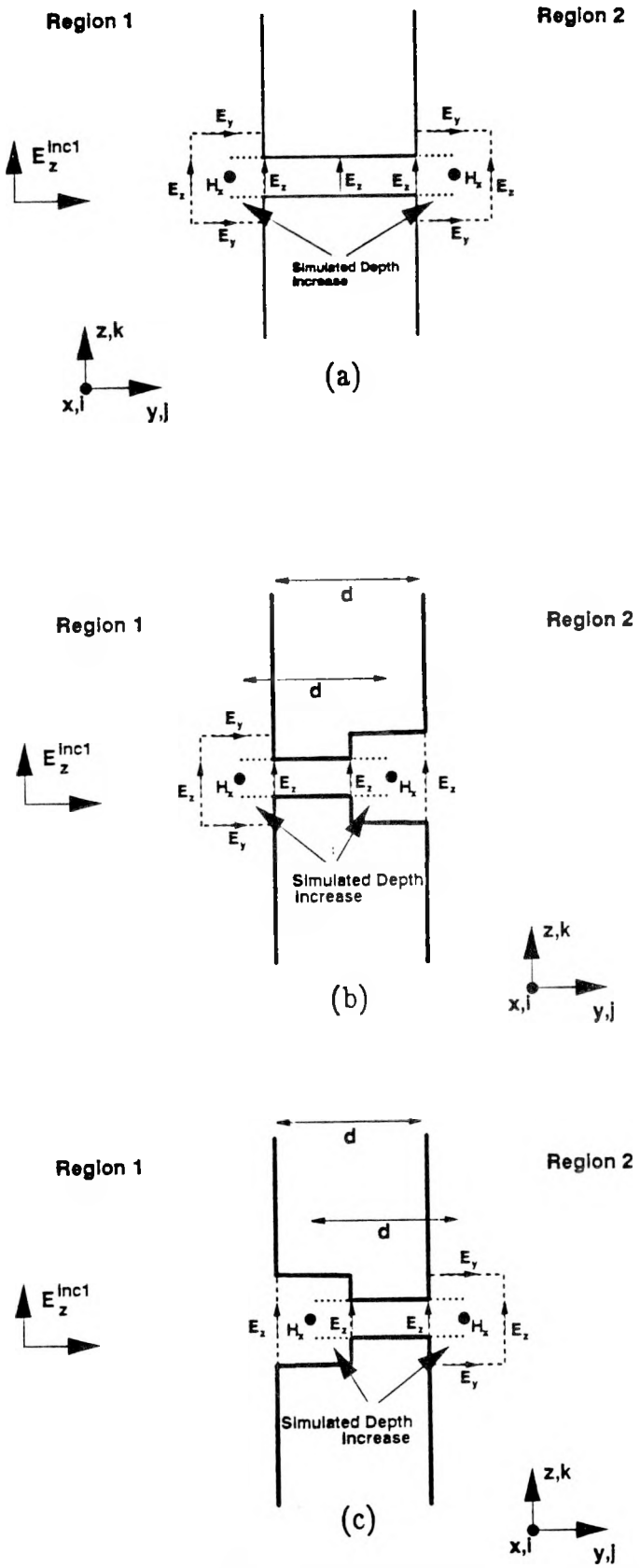

Fig. 15: Slots that result from an E-wall modeling approach. (a) Usual model that adds depth (ETSF); (b) Shifted model on rear face (Face 2 Shifted ETSF) ; (c) Shifted model on front face (Face 1 Shifted ETSF).

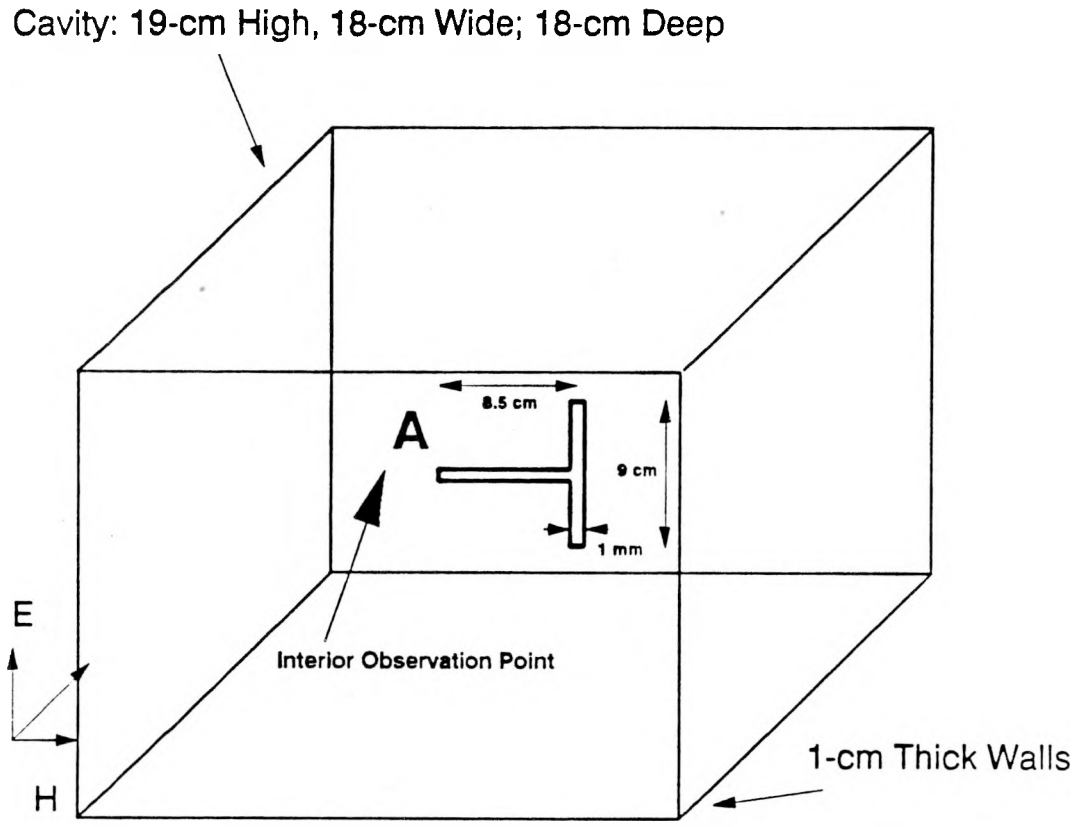

Fig. 16a: Tee-shaped slot coupling into a rectangular cavity driven by a z-polarized Gaussian pulse with a bandwidth of about 3 GHz and a peak amplitude of 1 V/m. FDTD cell is 1 cm.

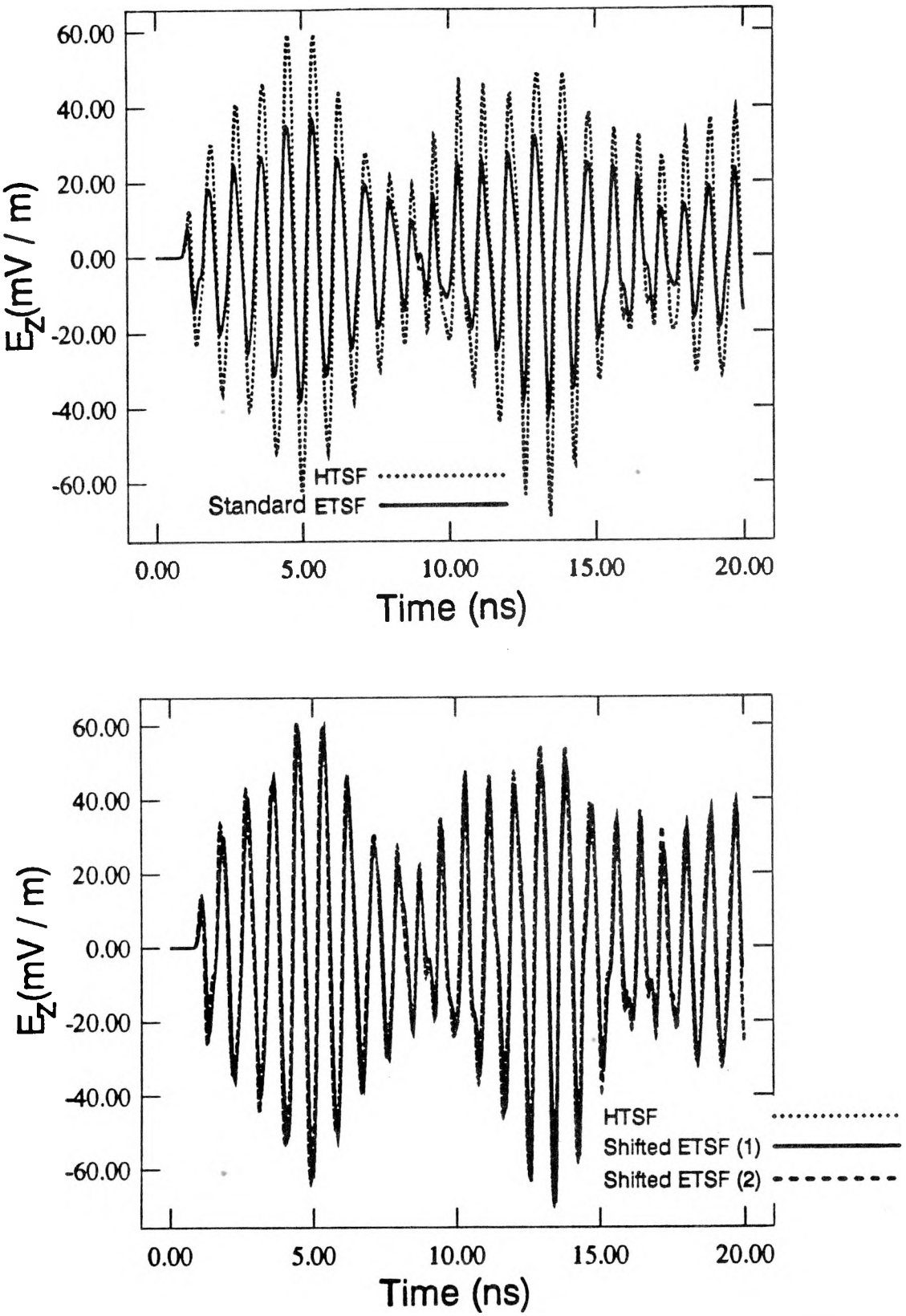

Fig. 16b: Results for an interior field based on the standard ETSF and the two Shifted ETSFs compared with the accurate HTSF. The number in parentheses denotes which face the shift was made on.

when an aperture is many cells deep and in this situation its accuracy is improved [11]. For providing comparison data for the HTSA, shifted ETSF results are used in this paper.

2.3 *Practical Considerations for Incorporating Thin-Slot Algorithms into TSAR*

The HTSA and the ETSF require modification of the standard FDTD **H**-field equations in those cells that are adjacent to the entering and exiting planes of the slot. Thus, provided the slot transverse **E** fields within these planes can be identified, the appropriate **H**-field equations that require modification are known (it is emphasized that only the transverse **E** fields are included). The technique for incorporating these algorithms into TSAR is dependent upon a data file that contains the following essential information:

SlotNum	Slot number with which each slot cell is associated
SlotCelI	i index of slot cell (x direction)
SlotCelJ	j index of slot cell (y direction)
SlotCelK	k index of slot cell (z direction)
SlotnDir	Direction of wall normal for slot cell (1=+x, −1=−x, 2=+y, −2=−y, 3=+z, −3=−z)
SlotComp	E-field component being flagged (1=$\mathbf{E_x}$, 2=$\mathbf{E_y}$, 3=$\mathbf{E_z}$)
SlotLoc	Location within wall for the slot cell flagged (0=in, 1=out)

These variables represent arrays that are used in the TSAR module, common.inc.

The SlotLoc parameter is defined to be 1 for "outer" slot cells and 0 for "inner" slot cells. For example, for a one-cell-thick wall defined on tangential **E**-fields (E–wall) all slot cells would have SlotLoc=1, because there are no **E**-fields interior to the wall in this case. If the slot were, in fact, many cells deep, the interior **E**-fields would be assigned SlotLoc=0, or would simply be omitted from the data file. For the more interesting case of a stair-stepped wall (Fig. 17), "outer" slot cells are those on outside corners; those on inner corners are not required for either the HTSA or ETSF and would be assigned SlotLoc=0, or could be omitted from the data file.

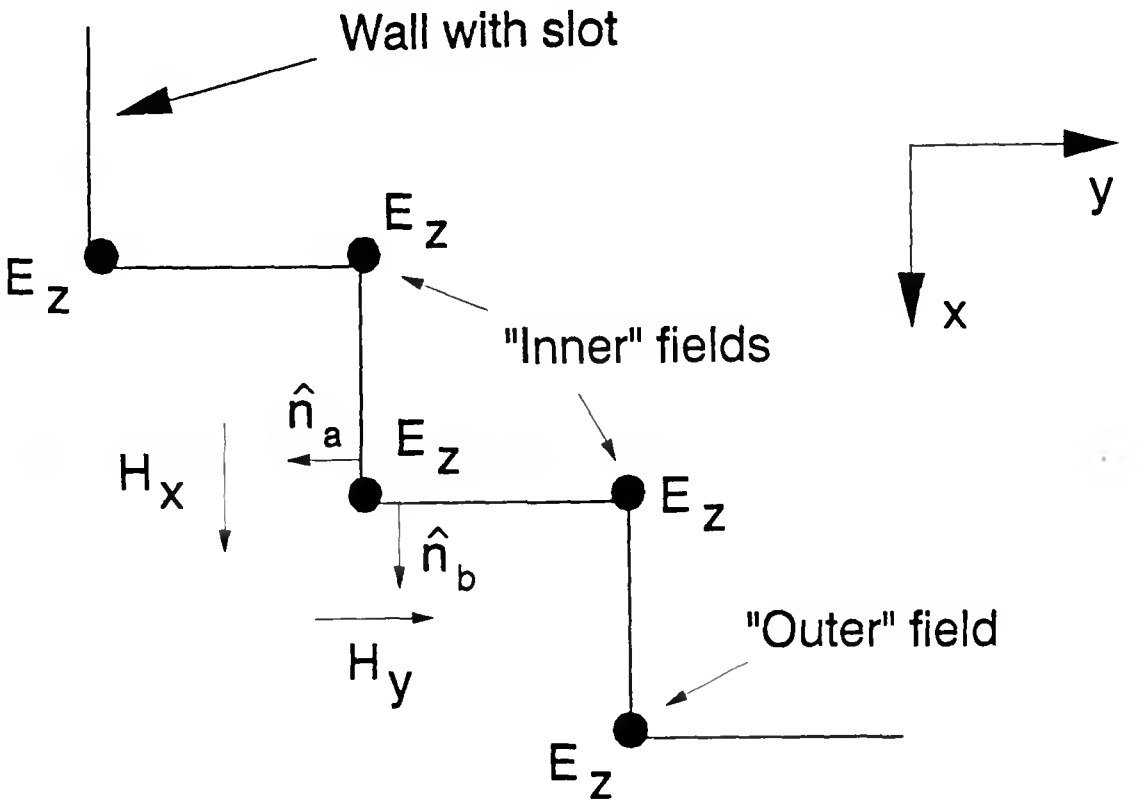

Fig. 17: Stair-stepped wall showing two possible normals. Slot is in the x-y plane. E_z denotes the transverse electric fields across the slot width.

Also shown in Fig. 17 is the existence of two possible wall normals that may be associated with the same flagged $\mathbf{E_z}$ field. These appear as two entries in the data file for this $\mathbf{E_z}$ field, each having the appropriate SlotnDir value.

One additional data line is required for each slot that includes the following:

SlotNtmp	Slot number (1,2,...)
SlotWid	Desired width of slot (meters)
SlotDep	Desired depth of slot (meters, HTSA only)
SlotMat	Material pointer for slot interior
Nseg	Number of subsegments per FDTD cell (HTSA only)
SlotAlgo	Algorithm to use for slot (1=HTSA, 2=ETSF)

The SlotDep parameter, as indicated, applies only to HTSA-defined slots. The depth of ETSF slots is determined by the actual gridding. The Nseg parameter also applies only to HTSA slots, and should be set to the value (4) for most calculations. This will yield 20 to 40 cells per wavelength for the integral-equation solution (the FDTD code is assumed to be using 5 to 10 spatial cells per wavelength). The value for Nseg may be set to an *even* integer greater than four if a high-resolution solution of the slot physics is required; however, the increase in CPU and memory overhead can be significant.

2.3.1 *Example Data File for a Diagonal Slot and Results for Several Slot Shapes*

In Fig. 18a is shown a diagonal slot. The wall containing the slot is assumed to be one cell thick. The front face is assumed to lie at the y-plane defined by j = 10, whereas the rear face is at j = 11. The outward normal on the front face is –y directed and is therefore assigned SlotnDir = –2; the rear face is assigned SlotnDir = 2. The data file for this slot could have the following form, with the row order non-essential (SlotNum, SlotCelI, SlotCelJ, SlotCelK, SlotnDir, SlotComp, SlotLoc):

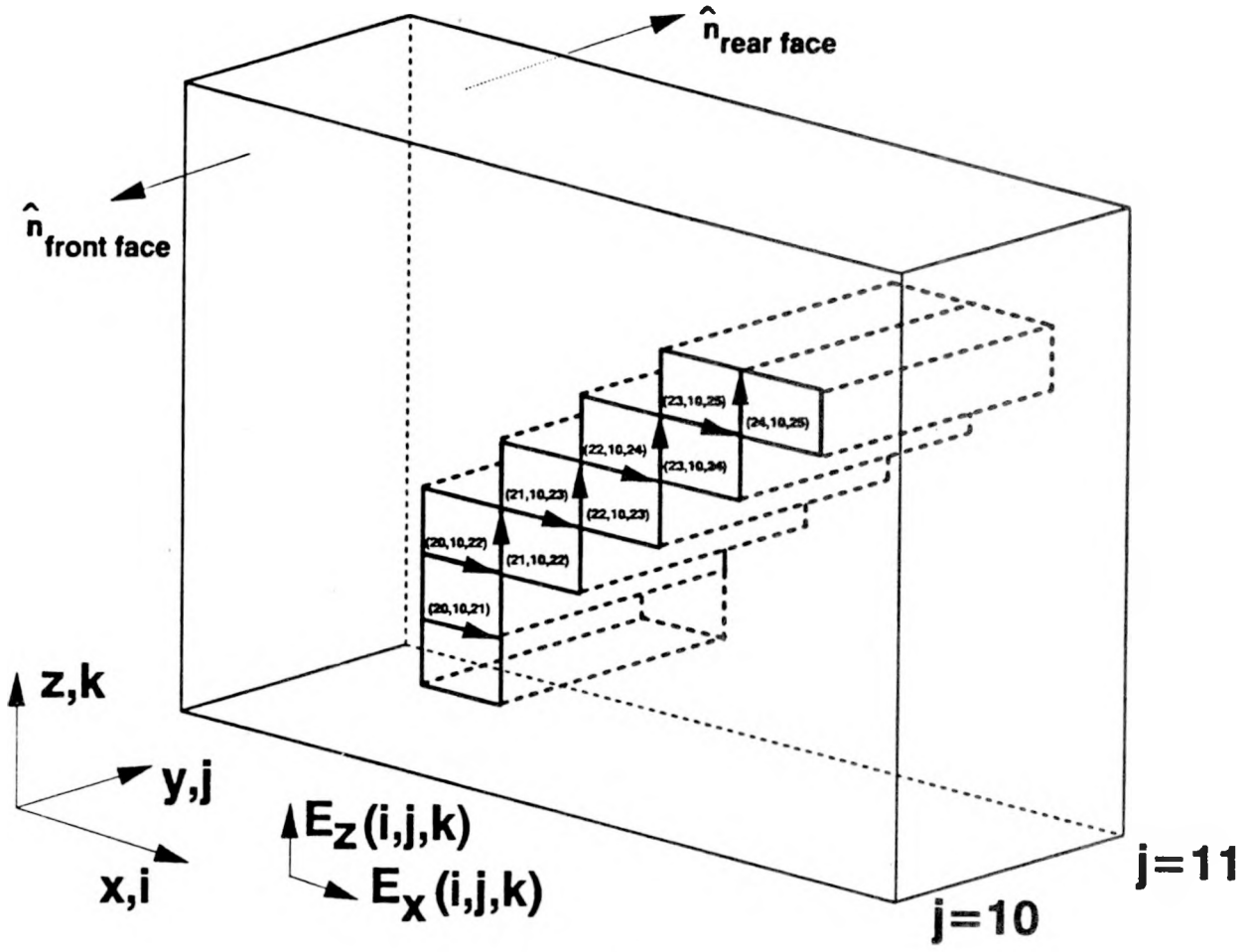

(a)

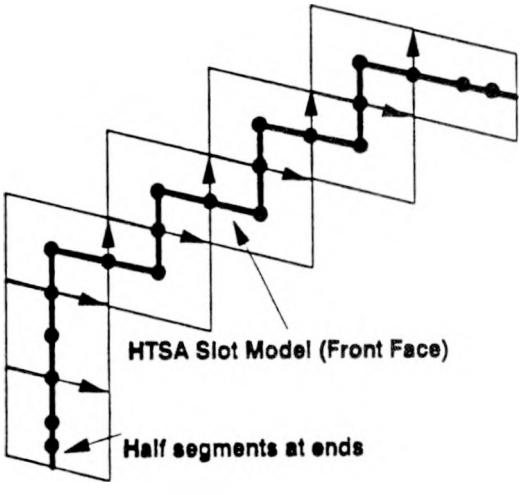

(b)

Fig. 18: Zig-Zag model of a diagonal slot showing FDTD cell indices and transverse **E** fields (a); (b) HTSA model that aligns with the FDTD E fields, but possibly adds many more nodes.

Slot #	I	J	K	nDir	Ecomp	Loc
1	20	10	21	−2	1	1
1	21	10	22	−2	3	1
1	22	10	23	−2	3	1
1	23	10	24	−2	3	1
1	24	10	25	−2	3	1
1	20	10	22	−2	1	1
1	21	10	23	−2	1	1
1	22	10	24	−2	1	1
1	23	10	25	−2	1	1
1	20	11	21	2	1	1
1	21	11	22	2	3	1
1	22	11	23	2	3	1
1	23	11	24	2	3	1
1	24	11	25	2	3	1
1	20	11	22	2	1	1
1	21	11	23	2	1	1
1	22	11	24	2	1	1
1	23	11	25	2	1	1

Slot #	Width	Depth	Mat	Nseg	Algo
1	0.001	0.01	1	4	1

The last row corresponds to the required information: SlotNtmp, SlotWid, SlotDep, SlotMat, Nseg, and SlotAlgo. The blank line after the cell-index data is required. The slots are assumed to be numbered consecutively, starting at one. Note that slot number 1 (SlotNtmp) is assumed to be 1 mm wide with a depth of 1 cm. The slot gasket material has been associated with material 1 (generally free space), and the HTSA algorithm has been flagged with four subsegments of the basic FDTD spatial distance. Alternatively, the ETSF algorithm could be used for this slot simply by changing the SlotAlgo entry to 2, but the depth would be restricted to the actual "griddèd" wall thickness. It is noted that the slot data file contains **E**-field information; however, the slot algorithms operate on **H**-field information that is internally obtained by a transformation. Figure 18b shows how the HTSA would model this slot for Nseg = 2. Additional nodes are added as Nseg increases.

A few comments are in order concerning the material pointer for the slot interiors. For the HTSA, the material pointer must have a double meaning: 1) It must indicate the desired values for the slot's relative permittivity and conductivity (EpsR and ConductE, respectively) so that these can be used by the HTSA routines;

and 2) It must force the slot to be shorted within the actual TSAR mesh. For the ETSF, the material pointer should also be to an appropriate EpsR and ConductE, but the E-fields defining the slot must *not* be shorted.

Figure 19 shows the diagonal slot coupling into an empty rectangular cavity with inner dimensions: 19-cm high, 18-cm deep, and 18-cm wide. The FDTD spatial cell size is assumed to be 1 cm. The illumination is a y-directed Gaussian pulse of the form $\exp[-\alpha\ (t-\beta)^2]$, where $\alpha = 6.79 \cdot 10^{19}$ and $\beta = 0.5 \cdot 10^{-9}$. The electric field is z polarized with unit peak amplitude.

Figure 20 compares HTSA and ETSF results for an interior $\mathbf{E_z}$ field at cell-index (23,22,26). In the time-domain, the two results are nearly identical up to about 5 ns and then modulation differences become apparent. The principal reason for the differences becomes obvious by examining the frequency spectra. The ETSF is showing that the dominant slot resonance is about 10–20 MHz (0.7% to 1.3%) lower than the HTSA result. A high-resolution integral-equation solution (Nseg=12) for the input impedance (cf. Section 2.2) places the dominant slot resonance at 1.53 GHz, which is very close to the HTSA solution in Fig. 20b. The 8–10 ns modulation on the transient results is due to the "beating" between this slot resonance and a cavity resonance at 1.418 GHz. The slightly higher HTSA resonant frequency yields a greater difference frequency and therefore a shorter modulation period. It is noted that a benefit of the HTSA formulation is that the slot depth can be arbitrarily defined, with the only restriction that it must be electrically small (less than about $\lambda/5$) at the highest frequency of interest.

The tee-shaped slot shown in Fig. 16a is again examined here. Each leg of the slot is redefined to be 0.1 mm wide for this example. Transient results for an interior $\mathbf{E_z}$ component based on HTSA and HTSF slot models are shown in Fig. 21. The illumination is the same as in the previous case. The agreement between the methods is seen to be generally very good, with some differences in the high-frequency content.

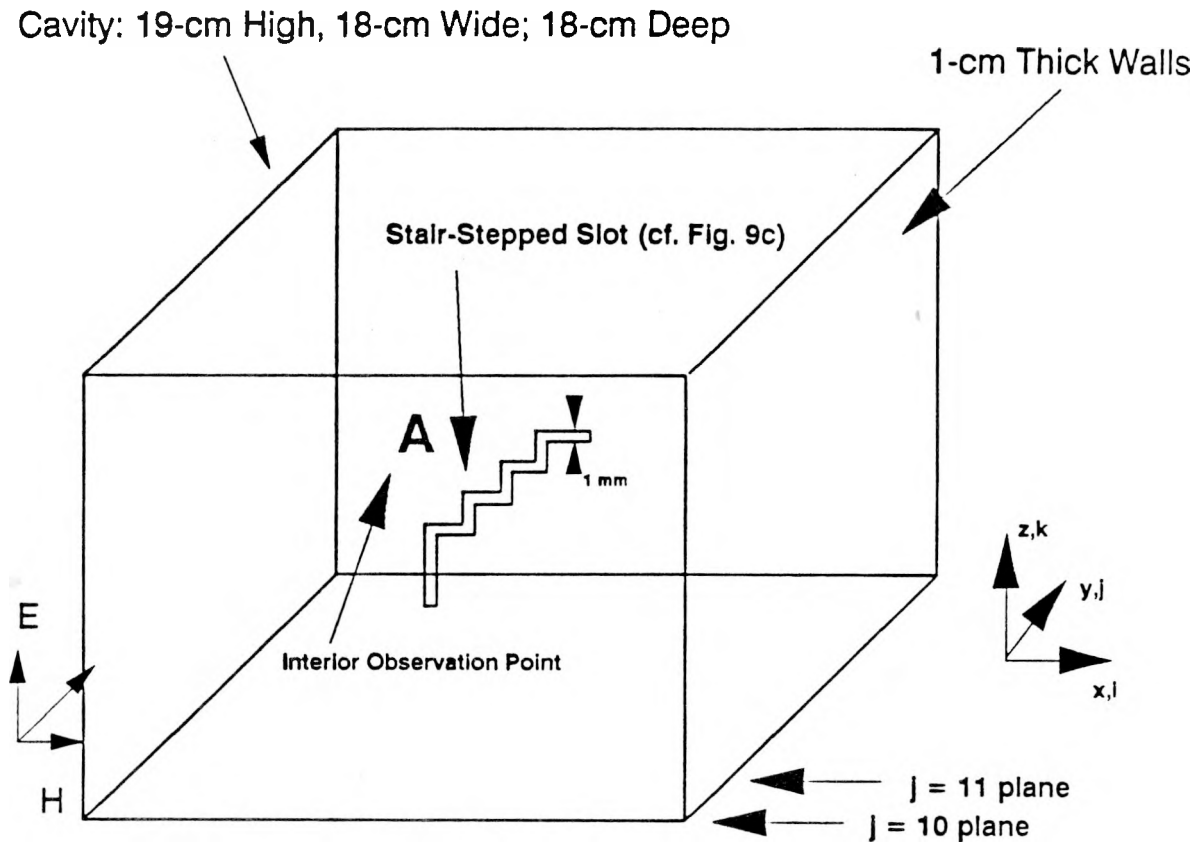

Fig. 19: Diagonal slot of Fig. 18 driving a rectangular cavity.

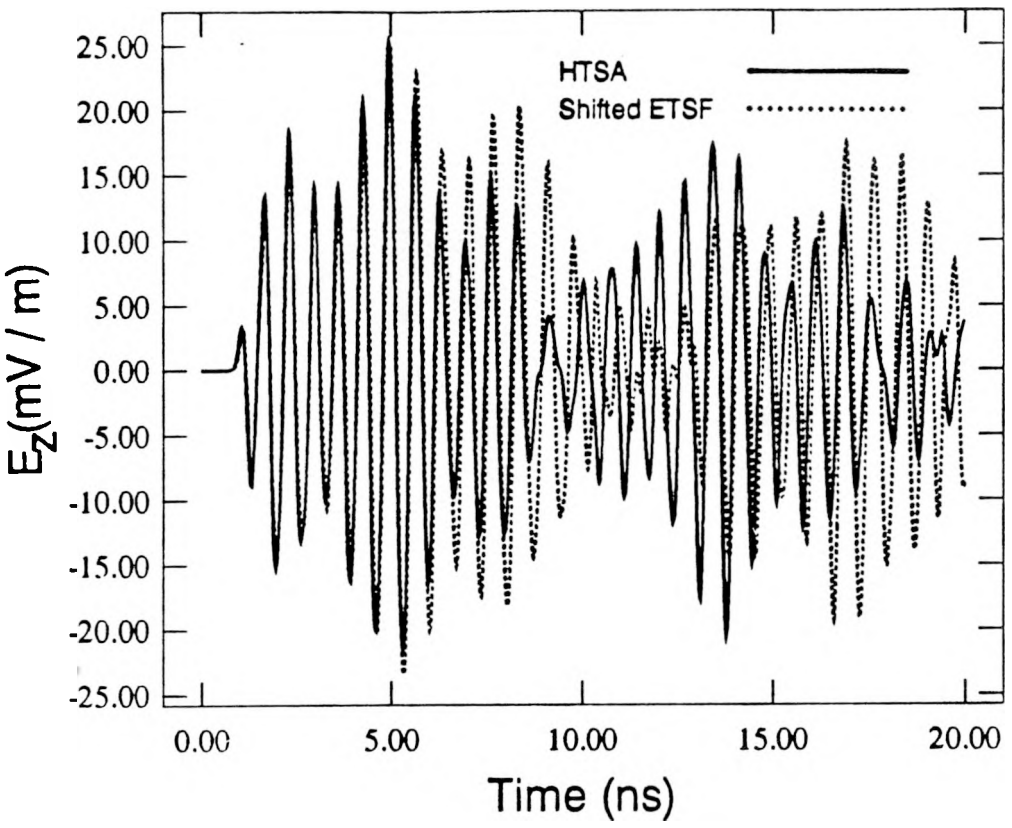

(a)

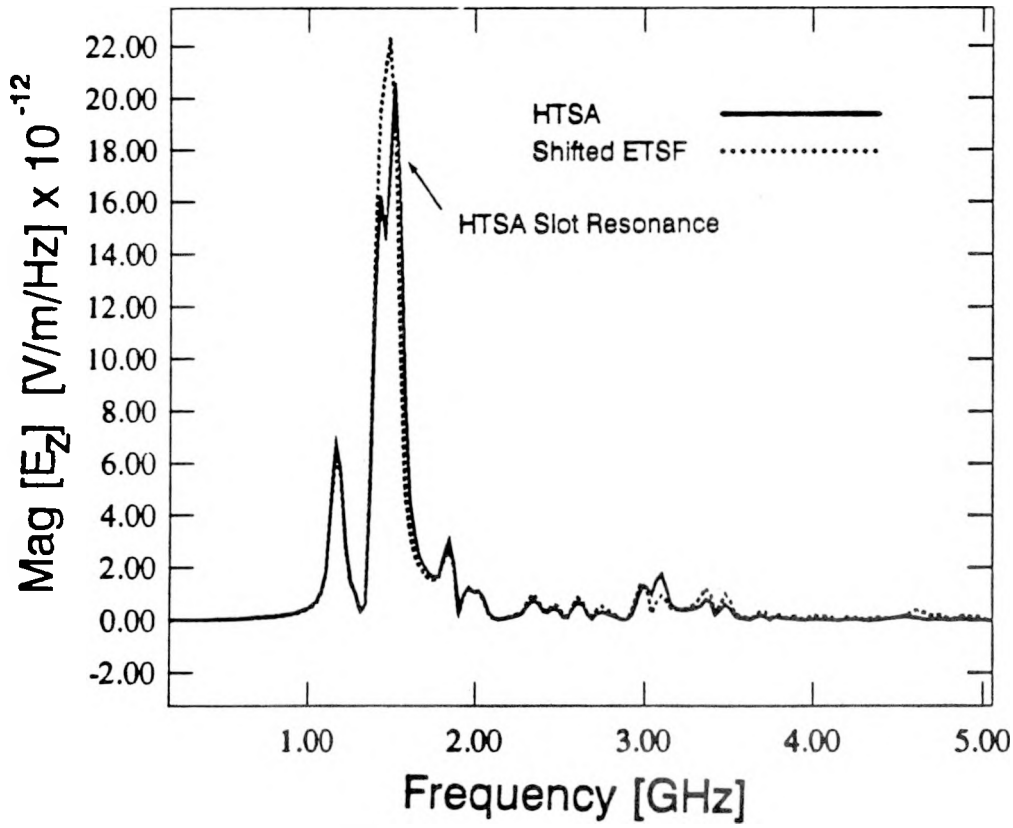

(b)

Fig. 20: Results for an interior E field based on a Shifted ETSF model and an HTSA model of Fig. 19. (a) Transient responses; (b) Transforms. FDTD cell: 1 cm.

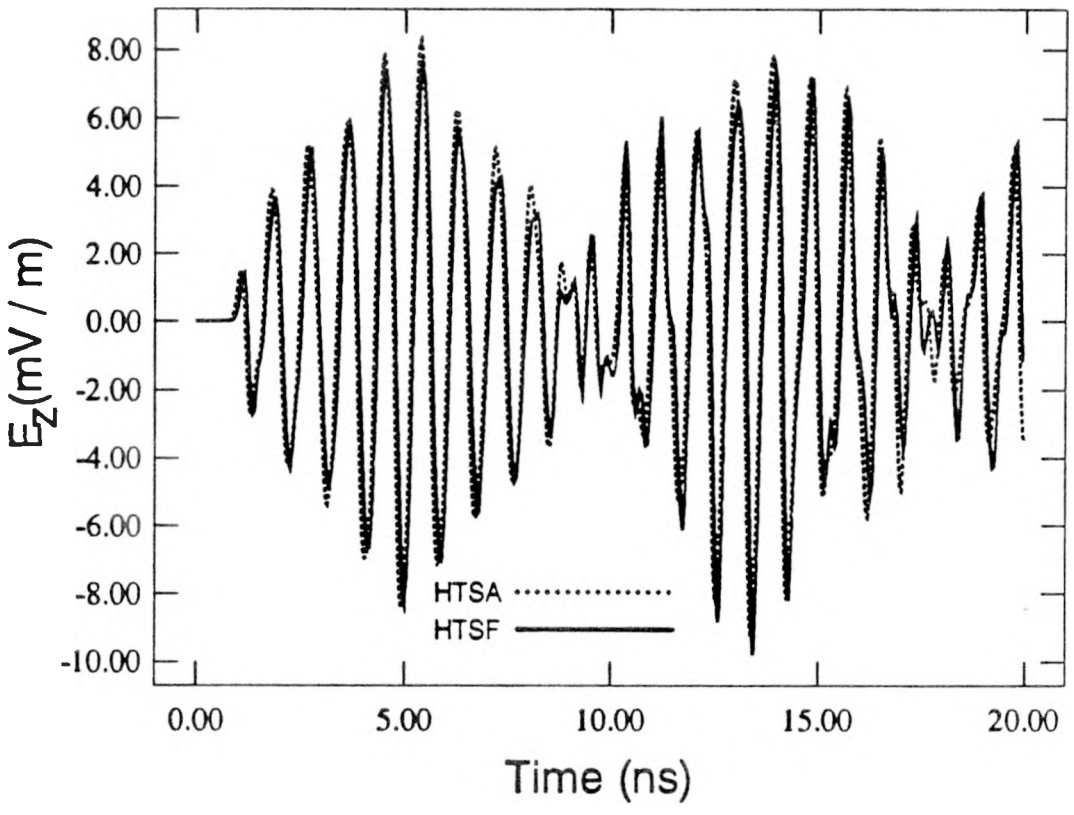

(a)

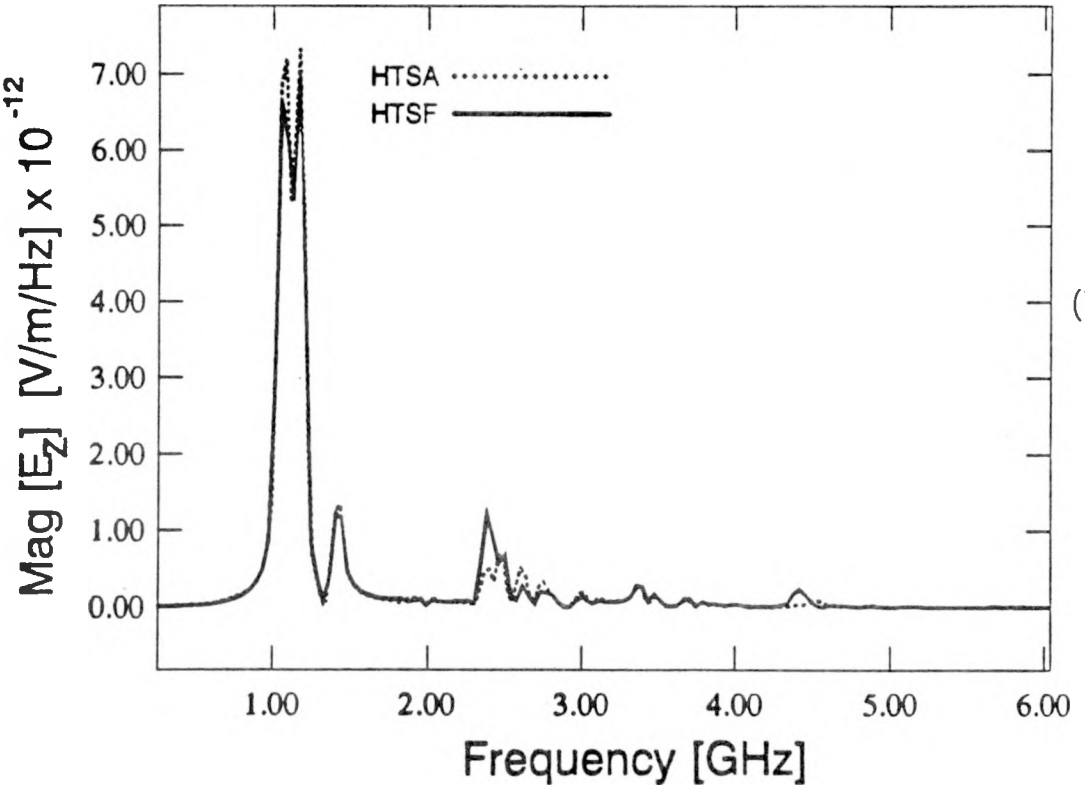

(b)

Fig. 21: Results for an interior E field based on an HTSF model and an HTSA model of Fig. 16a, but with the slot width changed to 0.1 mm. (a) Transient responses; (b) Transforms. FDTD cell: 1 cm.

A geometry that involves two boxes and two linear slots is shown in Fig. 22. HTSA and standard ETSF results for E_z in both the large and small cavities are shown in Figs. 23a and 23b (points A and B, respectively). The excitation is the same as in the previous examples. The HTSA result is based on a very low resolution solution of only eight basis functions for the long slot and four for the short slot. The agreement with the standard ETSF is very good, showing that this low-resolution HTSA formulation provides equivalent numerical accuracy to the ETSF for this case. Observe that this does not imply that either result has converged, but merely that the two approaches are consistent at this resolution. In fact, as the HTSA resolution is increased, modulation differences do appear.

A rectangular hatch aperture is shown in Fig. 24. The hatch is 0.1 mm wide, 1 cm deep and the illumination is the same as the previous examples. HTSA and HTSF results for E_z at an interior point are shown in Fig. 25a. Amplitude differences are seen in the two predictions after about 5 ns. Their Fourier transforms (Fig. 25b) reveal that the spectral content of the differences appear at about 1.4 GHz. The hatch has its dominant resonance at about 1.37 GHz (high-resolution method-of-moments prediction). A cavity resonance exists at 1.418 GHz. The HTSA is predicting a hatch resonance very close to 1.37 GHz, whereas the HTSF is predicting a slightly lower resonant frequency (10-20 MHz lower). Because the HTSA slot resonance is closer to the cavity mode, the HTSA result exhibits greater coupling to this mode; hence, the increased amplitude in later time.

The final example involves a 45°-degree rotated box, which leads to stair-stepped walls. To examine the type of accuracy that can be obtained for a stair-stepped geometry, a 10-cm-long, 1-cell-wide, 1-cell-deep linear slot was initially modeled on a box with faces that aligned with principal axes (Fig. 26a, no thin-slot algorithms used). The FDTD spatial cell was 1 cm. This box was then rotated 45° (Fig. 26b). Interior points were selected that correspond as closely as possible for the

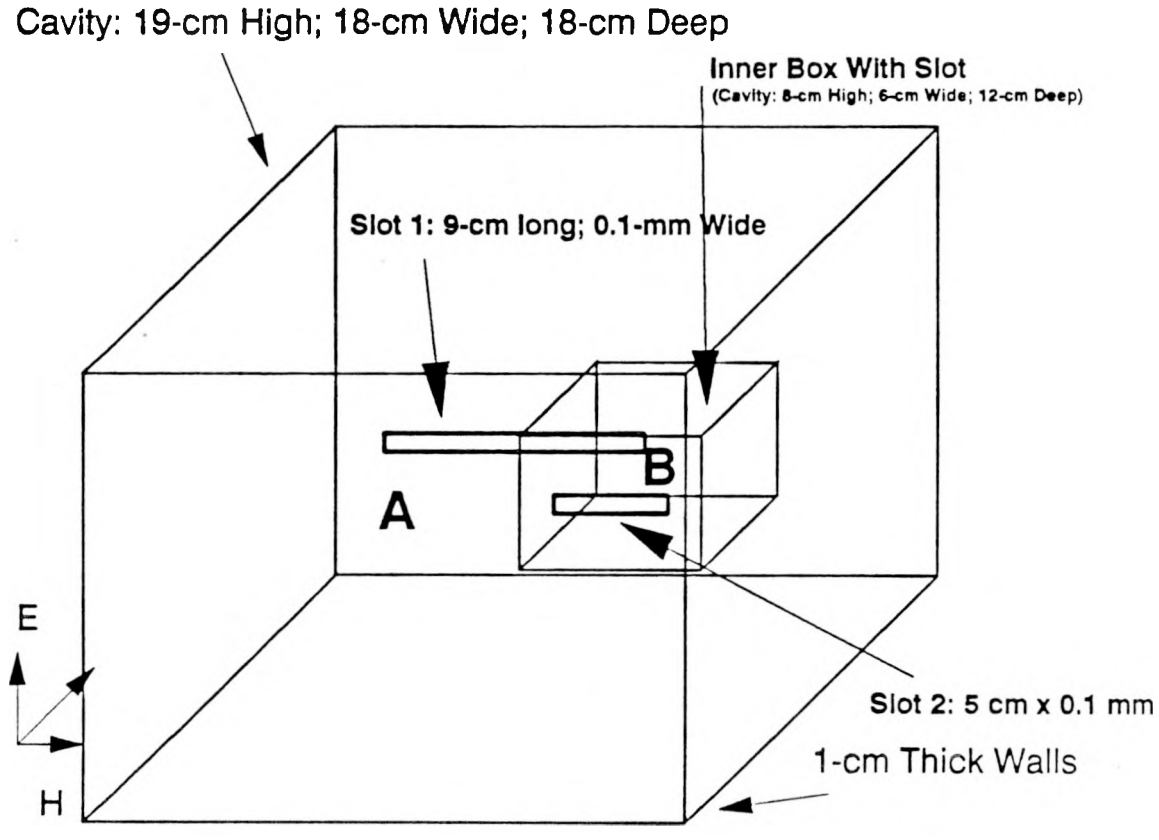

Fig. 22: Coupled linear slots. Point A is an observation point in the large cavity, whereas Point B is in the small cavity.

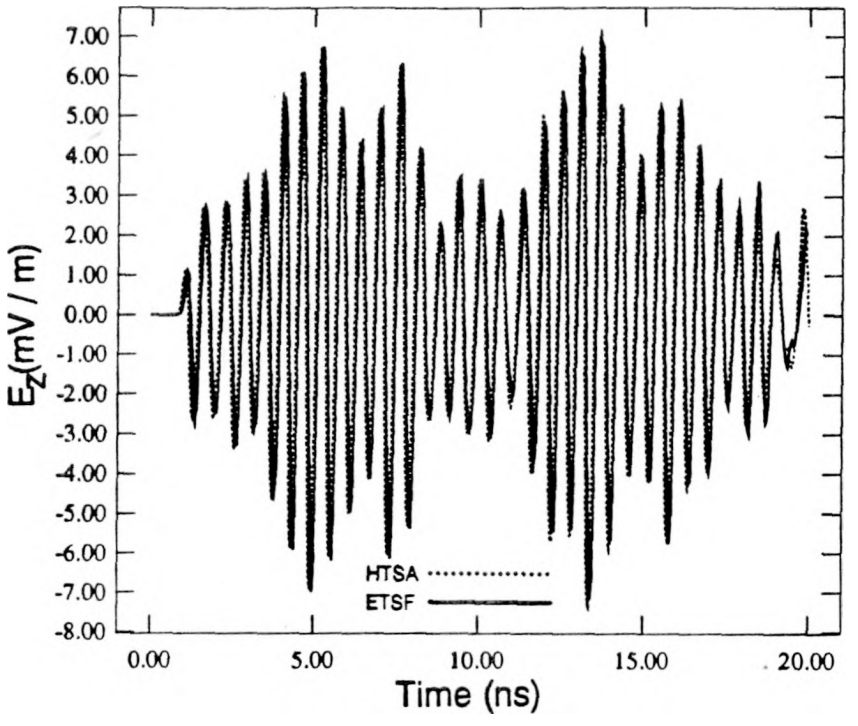

(a)

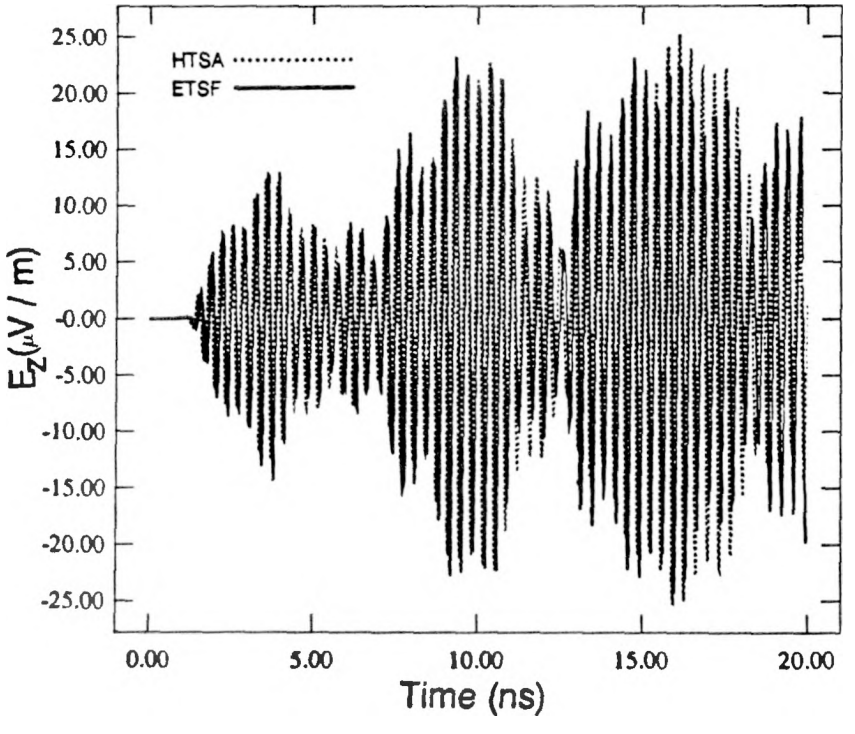

(b)

Fig. 23: Results for interior **E** fields based on a Standard ETSF model and an HTSA model of Fig. 22. HTSA model set d = 2 cm since comparing to Standard ETSF. (a) Transient response at Point A; (b) Transient response at Point B. FDTD cell: 1 cm.

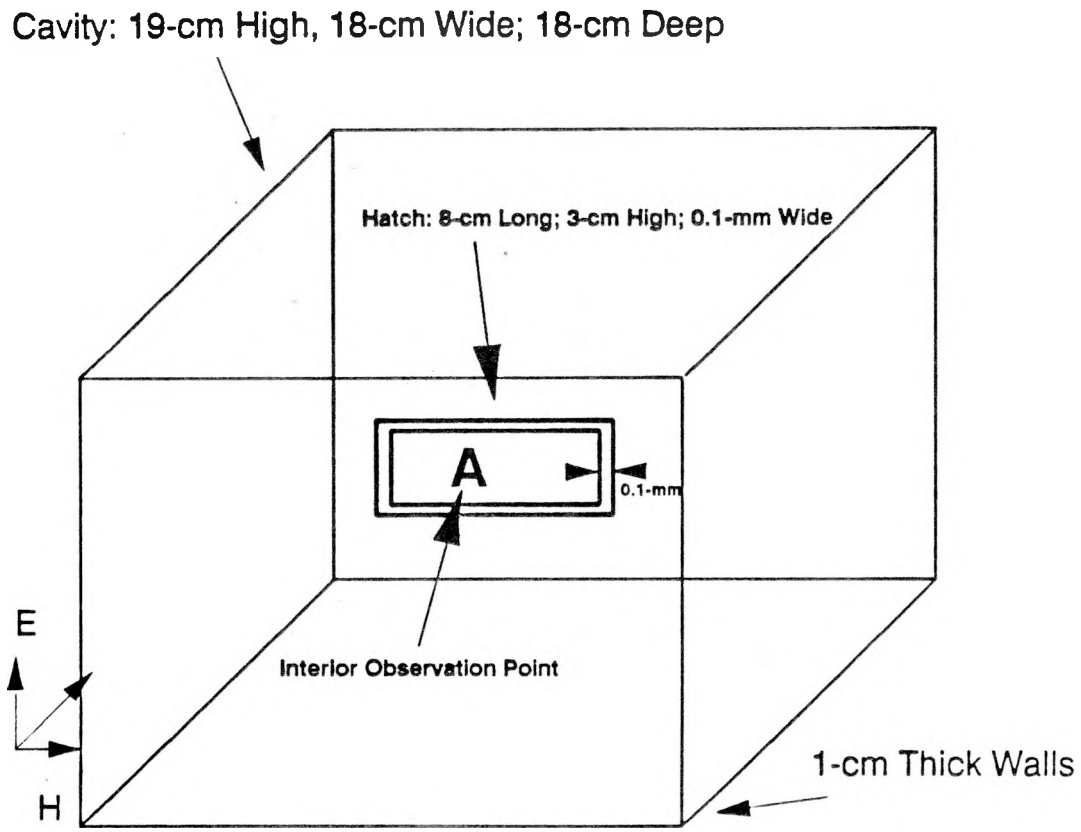

Fig. 24: Rectangular hatch aperture coupling into a cavity.

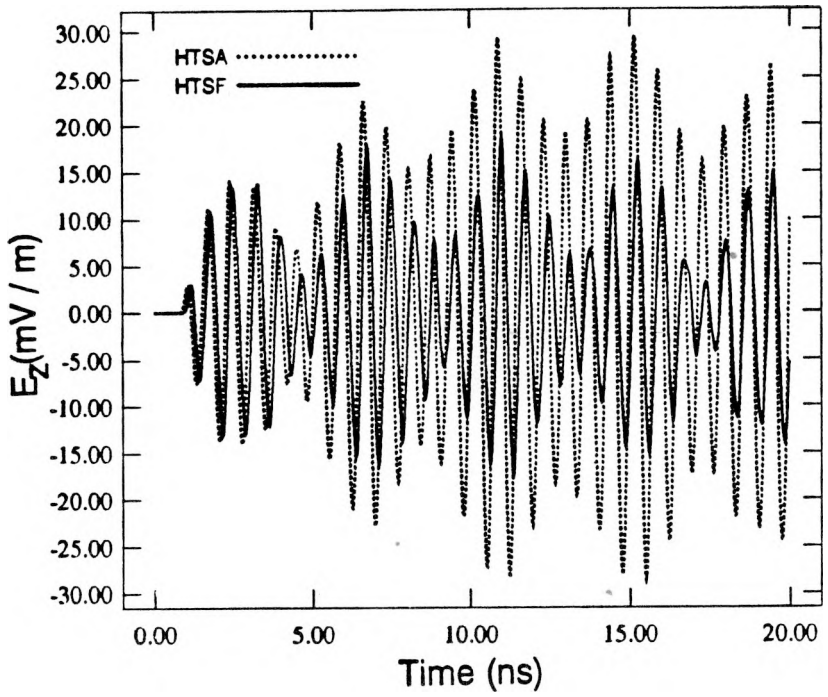

(a)

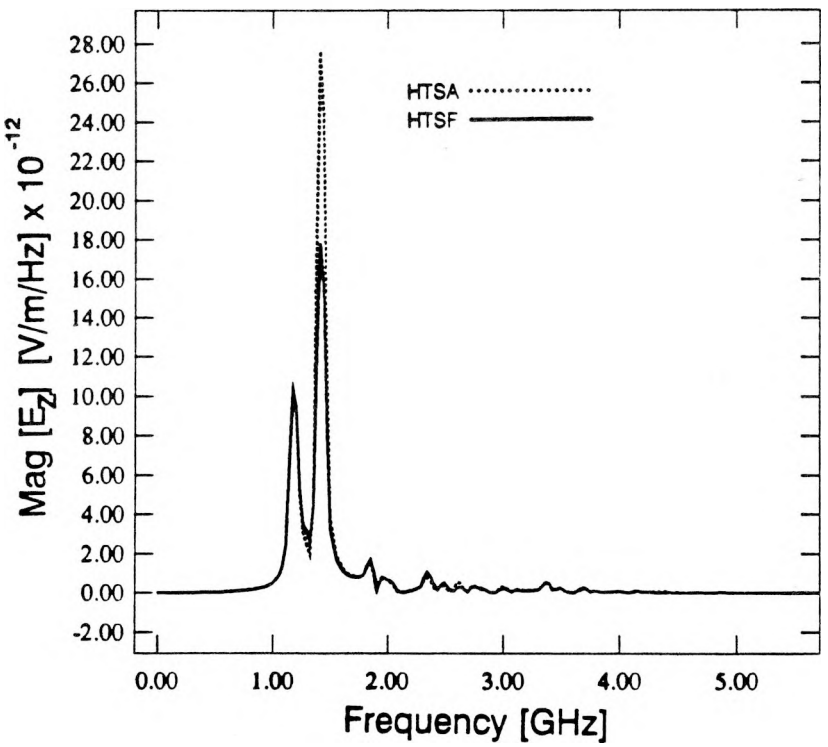

(b)

Fig. 25: Results for an interior **E** field based on HTSF and HTSA slot models of the hatch in Fig. 22. Slot depth 1 cm. (a) Transient response; (b) Transforms. FDTD cell: 1 cm.

CASE I: Box Aligned with TSAR Mesh

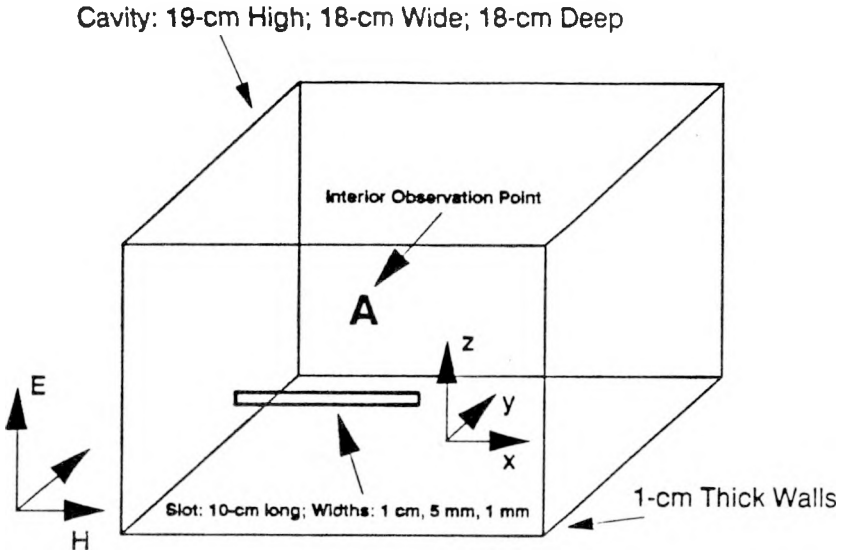

(a)

CASE II: Box Rotated 45°(Stair-Stepped Walls)

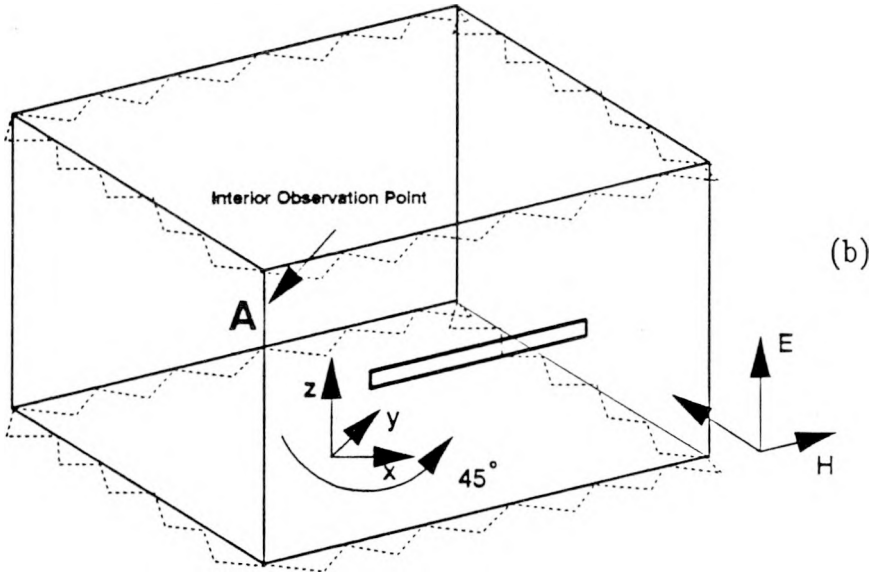

(b)

Fig. 26: Linear slot coupling into cavity for testing effects of stair-stepped walls. (a) Box and slot aligned with FDTD mesh; (b) Box rotated to yield stair-stepped walls.

two configurations. Figure 27a depicts results for $\mathbf{E}_z$ at these points. The excitation was broadside to the slot face for each case, using the previous Gaussian pulse. In principle, these results should be nearly identical; however, it is seen that considerable shifts in resonances have occurred. Notably, for the rotated case, the slot resonance has lowered by about 100 MHz, whereas the first cavity resonance has increased by about 100 MHz. The increase in cavity resonances implies that interior modes are following the minimum cavity dimension instead of the maximum,[5] and the lowering of the slot resonance is due to an increased path length on the upper and lower slot surfaces. These results show that stair-stepped walls, although they may not affect radar cross-section data significantly, clearly affect interior coupling problems when looking at specific interior field components. However, in a practical system assessment energy deposition is often the quantity of interest, and for this type of information the stair-step effects may be reduced. Additional study is required.

The ETSF thin-slot algorithm will work for non-grid-aligned walls; however, it will, of course, not offer any correction for the inherent limitations associated with the Yee cell. In Figure 27b is shown the spectra for $\mathbf{E}_z$ at the same interior point for three slot widths in the rotated configuration: 1 cm wide, 5 mm wide, and 1 mm wide (1-cm fixed FDTD cell size). The expected decrease in amplitude is observed. Note, also, that the slot resonance decreases in frequency with decreasing slot width, which is contrary to linear slots on planar walls, but consistent with diagonal (zig-zag) slots on planar walls. Note that for the 1-mm-wide case, the distinction between the slot resonance and the first cavity resonance is not resolved by the transform. In Figure 28 is shown the spectra for the 1-mm-wide slot on the rotated box compared to a 1-mm-wide slot on a non-rotated box. The differences are substantial; however, they are

[5]Because of the stair-stepped walls, the minimum interior diminsions are 19-cm high, 16.97-cm wide and 16.97-cm deep, whereas the maximum interior dimensions are 19-cm high, 18.38-cm wide, and 18.38-cm deep.

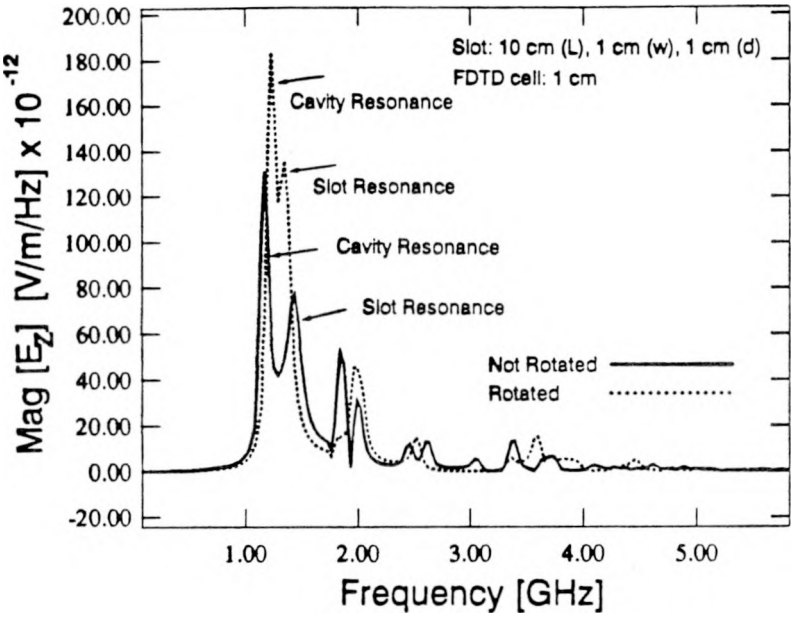

(a)

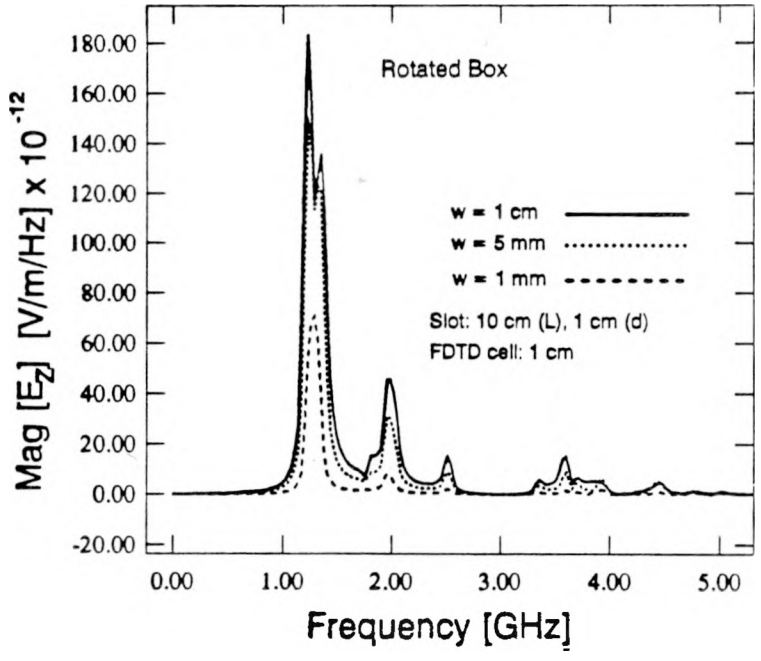

(b)

Fig. 27: Interior E-field results for the rotated and non-rotated boxes of Fig. 26. (a) Fully gridded solutions for a 1-cell-wide slot; (b) ETSF application to reduce slot width on the rotated box. FDTD cell: 1 cm.

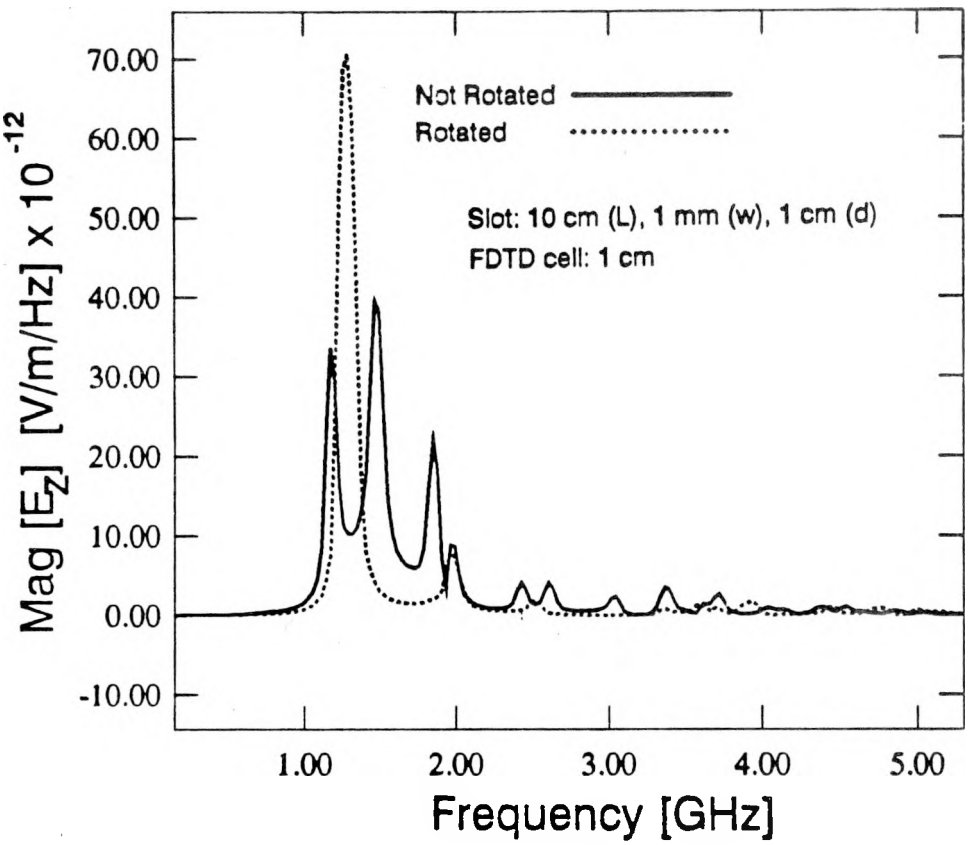

Fig. 28: Interior **E**-field results for the rotated and non-rotated boxes of Fig. 26, but with a slot width of 1 mm and an FDTD cell of 1 cm. For the non-rotated result, the Shifted ETSF was used. For the rotated case, the standard ETSF was used due to poor definition of the slot length and depth.

consistent with the similar results for the fully gridded, 1-cell-wide case shown in Fig. 27a, which demonstrates the inherent problems associated with non-axis-aligned walls. These results demonstrate that every effort should be made to ensure that apertures fall on planar walls if very accurate results are required for specific interior fields (it is recognized that this will not always be possible).

2.3.2 *Listing of TSAR Modules Added or Modified for The HTSA and ETSF*

The new routines that have been added to TSAR to implement the HTSA and ETSF algorithms include:

initslot.f:
Called from readinit.f, this routine now reads the slot data file and the HTSA slot initialization, if required.

loadslot.f:
Call from tsar.f for every y-plane, this routine appends the HTSA magnetic currents, K_x, K_y, or K_z from the previous time step to the appropriate $\mathbf{H_x}$, $\mathbf{H_y}$, or $\mathbf{H_z}$. This routine also stores $\mathbf{H_x}$, $\mathbf{H_y}$, and $\mathbf{H_z}$ as slot drivers for the slot solution at the next time step (used by solvslot.f)

solvslot.f:
Called from tsar.f every time step, this routine contains the HTSA solver.

etsfhx.f:
Called from advhx.f, this routine applies the ETSF to $\mathbf{H_x}$ slot drivers, if appropriate.

etsfhy.f:
Called from advhy.f, this routine applies the ETSF to $\mathbf{H_y}$ slot drivers, if appropriate.

etsfhz.f:
Called from advhz.f, this routine applies the ETSF to $\mathbf{H_z}$ slot drivers, if appropriate.

The following TSAR routines have been changed to accommodate the HTSA and ETSF algorithms:

common.inc:

The vast majority of required new common variables are defined at the end of the original file. Additional changes throughout the module include: 1) The INTEGER declaration of the parameters MaxSlots, MaxSlCls, MaxNodes and NHistory; 2) The addition of the logical unit number LunSlot = 10 for the slot data file; 3) The declaration REAL*8 for the TSAR variables Dt and Dx (this is required when the HTSA is run on 32-bit processors; cf. Section 2.3.3)

tsar.f:

The main TSAR routine has been changed to call the appropriate subroutine for HTSA slots, if required.

readinit.f:

This routine has been changed to call initslot.f during all of its normal initialization calls.

advhx.f:

This routine has been changed to call etsfhx.f for ETSF application, if required.

advhy.f:

This routine has been changed to call etsfhy.f for ETSF application, if required.

advhz.f:

This routine has been changed to call etsfhz.f for ETSF application, if required.

defaults.f:

Several flags associated with the HTSA and ETSF algorithms are initialized here.

done.f:

This routine now prints the energy received by each HTSA slot at the end of the calculation, if requested through the flag FlagENGY.

initlvl2.f:

This routine has been changed to delay the storing of $\mathbf{H_y}$, along with $\mathbf{H_x}$ and $\mathbf{H_z}$, until the next y-plane. This is necessary in case a requested $\mathbf{H_y}$-sensor happens to be one of the slot drivers for an HTSA slot.

params.inc:

The maximum number of thin slots is defined by MaxSlots.

The maximum number of nodes for each slot is defined by MaxNodes. This is generally chosen to be about 30 % larger than Nseg times the number of TSAR cells in the longest slot.

The parameter MaxSlCls must be set at least as large as the total number of field points in the slot data file; however, the HTSA will internally flag additional TSAR cells that fall at the ends of open-ended slots. Thus, a realistic minimum value for MaxSlCls is the total number of cells in the data file, plus the number of open ends for HTSA defined slots.

The maximum number of time steps that can be retained for each slot is defined by NHistory. Note that because of the nature of transient integral-equation solutions, a time history dictated by the retarded time *must* be retained. A crude minimum value for NHistory is 2·MaxNodes.

NAMELIST user input file (named in params.inc):

The flag FlagSlot is set to .TRUE. if any thin slots exist in the problem (if no thin slots exist, FlagSlot must be set to .FALSE.). The flag FlagENGY is set to .TRUE. to calculate the received energy for each HTSA slot. The name of the slot data file is specified in the variable SlotFile.

2.3.3 *Miscellaneous Application Limitations and Implementation Details for the HTSA*

Application of the HTSA is limited to regions that are truly planar local to the slot. In other words, all flagged fields in the slot data file for a particular slot must have the same *absolute value* of SlotnDir. Observe that this does not mean that HTSA slots can exist only on large x-z, y-z, etc., planes, but it does force the wall region local to the slot to be flat. The HTSA examines the values for SlotnDir, and will not run if the slot is non-planar; however, the ETSF algorithm can be used for non-planar slots.

In the present release, each numbered HTSA slot must be a single, continuous entity, and all slots must be spatially separated by at least one FDTD cell so that only one slot falls within a single FDTD cell. For example, two parallel linear slots must be defined as two separate slots in the slot data file to avoid mutual interaction between the slots being account for twice. This is because the integral-equation solution will account for the interaction once and the FDTD feedback technique will account for it again, giving unpredictable results. However, in principle, the HTSA can accommodate multiple parallel slots falling within the *same* FDTD cell by letting the integral equation account for all mutual interaction that cannot be resolved by the FDTD code. This interesting extension will be incorporated in future releases.

The electrical depth of the slot at the highest frequency of interest must also be examined with the HTSA because the algorithm inherently assumes that the

transverse electric field is uniform through the slot depth. Although the HTSA is effective for slots that may be one, or perhaps two FDTD cells deep, it is primarily intended for slots that are less than one FDTD cell in depth. Indeed, no other existing thin-slot algorithm provides similar accuracy for this case [11], whereas the deep-slot case may be handled by the ETSF.

The HTSA requires that the material located one FDTD cell outside the slot be free space, but the material inside the slot may have a specified relative permittivity and conductivity (but non-magnetic). These limitations will be relaxed in future releases of the HTSA, along with the inclusion of internal wall-loss effects. An obvious requirement of both the HTSA and the ETSF is that the walls that contain the narrow slot are of high conductivity.

The numerical stability of the HTSA solution may pose difficulty for some complex aperture configurations. Every effort has been made to trap situations that are known to yield stability problems, including: 1) Four or more slots that merge at a single junction have been found to yield unpredictable stability problems; thus, a maximum of three slots can merge at a single junction in this release; and 2) The equivalent radius must be less than or equal to one-tenth of the FDTD spatial cell size. This latter condition is only serious for slots with zero depth, where the width would have to be less than or equal to 0.4 times the FDTD cell; e.g., for an FDTD cell of 1-cm, the maximum slot width for a slot with zero depth would be 4 mm (cf. Eq. (3) to determine the equivalent radius).

The convergence of the integral-equation solution can be a minor problem for very complex slot shapes, resulting in the dominant resonance being as much as 3% higher in frequency than the "correct" resonant frequency. This is not a deficiency of the hybrid approach as much as a limitation of existing techniques to numerically solve the electric field integral equation. The resulting error for a given number of basis functions is, of course, dependent on the specific form of the basis functions. The

piecewise-linear (triangular) functions used here are not as accurate as, say, piecewise sinusoids; however, using the latter is expected to complicate the solution procedure (further study is required). A well-known "trick" to reduce the error of low-resolution solutions applied to open-ended structures is to slightly extend the length of the model [13]. For the HTSA, one quarter of the slot's maximum spatial delta (uniform TSAR spatial delta assumed) is appended to each open end such that the sum over all slot segments does not increase by more than 2½ %. This is only done for slots that contain right-angle bends, and has been found, in general, to yield the dominant resonance within about 1% of very high-resolution solutions (> 120 nodes per wavelength). It is interesting to note that the FDTD technique based on the Yee mesh is often able to obtain similar accuracy using only 5 to 10 cells per wavelength! Of course, such small errors are not likely to be significant in a practical system assessment, but they are important for academic purposes.

The HTSA solves the slot problem on a plane, but when used in a general three-dimensional FDTD code this plane may fall anywhere in space. Thus, the solvslot.f module initially defines a new local coordinate system, and then lays out the slot basis functions for each face of the wall that contains the slot. Note that because of the randomness with which the slot data file may be created, the basis-function indices for each face may not be one-to-one; e.g., node 5 on one face may not be at the same relative slot position as node 5 on the other face. To properly create pointers to the FDTD fields, a correlation vector between the faces is generated. These implementation complications are unique to the HTSA because of the inherent differences associated with the offset-FDTD and integral-equation techniques.

To improve the stability of the HTSA, the solution considerably sub-steps TSAR both in space and time. The degree of sub-stepping increases with the choice of Nseg. For example, when Nseg is set to four the HTSA spatial delta is one fourth of

the spatial step used in TSAR, whereas the time step is defined to be one eighth of TSAR's value. Thus, for each TSAR time step the HTSA makes eight advancements. Because of the excessive computation, the HTSA uses look-up tables for the appropriate Green's functions and retarded-time indices, which are generated when initslot.f is called. This drastically improves execution speed, but at the expense of memory overhead. The decision to adopt this approach was based on the fact that today multi-megabyte systems are commonplace. For typical problems that involve one or two thin slots, each with perhaps 100 to 200 nodes, the HTSA will introduce 2 to 5 megabytes of additional storage requirements. The examples in this paper generally used Nseg = 4, which resulted in only a 5 to 10 percent increase in TSAR's execution time. However, increasing Nseg to eight could easily result in a doubling (or more) of the execution time. For this reason, Nseg = 4 is recommended.

The HTSA was written assuming the code will be run on 32-bit processors, such as a SUN SPARCstation. On this class of machine, TSAR runs in single precision (i.e., REAL*4). The HTSA requires double precision (REAL*8) when initializing the look-up tables, and therefore, often uses REAL*8 declarations. The TSAR-specific variables Dx and Dt are affected by this precision increase, and therefore these variables MUST be declared REAL*8 in the module common.inc. If the program is to be run on a 64-bit machine such as the CRAY, all REAL*8 declarations should be changed to REAL. In addition, the critical inner loop in the HTSA can be made to vectorize on the CRAY, which improves performance considerably. The alternate form of this loop should be uncommented for this application (this is defined in the HTSA source code).

3. CONCLUSIONS AND AREAS FOR FURTHER STUDY

The HTSA and ETSF techniques for modeling very narrow apertures in the FDTD code, TSAR, have been successfully automated based on a "slot data file" that identifies those cells within the FDTD mesh that are to contain a thin slot. The flagged cells are based on **E** fields, along with outward-normal unit-vector information. The Lawrence Livermore National Laboratory is modifying TSAR's graphical interface so that the appropriate data file is generated after the slot is defined at the solid-model level. A "user's manual" to the algorithms will follow the interface development.

The HTSA is based on an integral-equation solution for the slot problem and uses both the slot depth and slot width as free parameters, with the restriction that these must be electrically small at the highest frequency of interest. The method is only applicable to slots that fall on truly planar walls. An interesting feature of the HTSA is that it is not bound to the spatial and time steps used in the main FDTD code, and therefore, a very high-resolution solution of the slot is possible (although a substantial increase in overhead can result).

The ETSF algorithm is geometrically more flexible than the HTSA; however, the slot depth is bound to the actual FDTD mesh. In addition, previous studies have shown that the ETSF in its standard form adds apparent depth to the slot which results in an underestimation of the aperture fields [11]. By applying the ETSF to a planar based slot that is assumed to be simply one-cell narrower in depth, the apparent depth increase can often be avoided. This results in an experimental *shifted* ETSF. This method remains under investigation at this time, and consequently, only the standard ETSF has been incorporated into TSAR. Although the standard method adds depth to the slot that can lead to aperture fields being underestimated by as much as a factor of two for slots that are one-cell deep and very narrow, its accuracy improves as cells are added to the slot depth [11]. In addition, the method can also be

used for non-planar slots. The only existing technique that could solve these cases more accurately would be the HTSF, but automating this method would be very awkward because entire walls must be shifted so that they fall on tangential $\mathbf{H}$ fields as opposed to $\mathbf{E}$ fields.

The HTSA and ETSF methods are designed to compliment each other so that a particular problem can model one slot using the HTSA, while another uses ETSF. This possible mixing of algorithms has been built into the thin-slot package.

Some areas for additional study of the narrow-slot problem in FDTD codes are the following: 1) Further investigate driving the FDTD mesh with the HTSA magnetic currents for the case that the HTSA segments do not align precisely with FDTD electric-field points (this would enable a diagonal slot to be modeled as being truly diagonal instead of a stair-stepped approximation); 2) Further improve the convergence characteristics of the finite-difference solution of the HTSA integral equation; 3) Examine the possibility of using the HTSA on stair-stepped walls; 4) Further study the modeling improvements associated with the shifted ETSF; 5) Contour methods fail for slots that are not an integer multiple of the FDTD spatial cell due to constant-field assumptions made in Ampere's law; thus, modification of the curl-$\mathbf{H}$ equations in the slot may improve this deficiency; 6) Add wall-loss features to the HTSA model [22]; and 7) The thin-slot algorithms have been written to be compatible with the paging scheme that TSAR uses to solve large, "out-of-memory" problems; however, due to time constraints, this has not been verified.

Some additional areas for overall improvement to the TSAR modeling system could include: 1) Automate thin-wire modeling capabilities; 2) Examine the possibility of modeling shielded wire bundles (multi-wire cables) through a hybrid transmission-line/FDTD model; 3) Add radar cross section capabilities that account for frequency-dependent surface loss; 4) TSAR and the HTSA are written based on a uniform spatial step; permitting different spatial steps in different directions would add flexibility.

REFERENCES

[1] K.S. Yee, "Numerical solution of initial boundary value problems involving Maxwell's equations in isotropic media," *IEEE Trans. Ant. Prop.*, vol. AP–14, pp.302–307, May 1966.

[2] R. Holland, "THREDE: a free-field EMP coupling and scattering code," *IEEE Trans. Nucl. Sci.*, vol. 24, 6, pp. 2416–2421, Dec. 1977.

[3] A. Taflove, "Review of the formulation and applications of the finite-difference time-domain method for numerical modeling of electromagnetic wave interactions with arbitrary structures," *Wave Motion*, vol. 10, 6, pp. 547–582, 1988.

[4] D. Sullivan, "Three-dimensional computer simulation in deep regional hyperthermia using the finite-difference time-domain method," *IEEE Trans. MTT*, vol. 38, 2, Feb. 1990.

[5] R.R. McLeod, "Temporal Scattering and Response Software User's Manual, Ver. 2.1 (R)," Lawrence Livermore National Laboratory, Tech. Rept. UCRL–MA–104861, Livermore, CA, Sept. 1990.

[6] J. Gilbert and R. Holland, "Implementation of the thin–slot formalism in the finite–difference EMP code THREDII," *IEEE Trans. Nucl. Sci.*, vol. NS–28, 6, pp.4269–4274, Dec. 1981.

[7] A. Taflove, K.R. Umashankar, B.Beker, F. Harfoush, and K.S. Yee, "Detailed FD–TD analysis of electromagnetic fields penetrating narrow slots and lapped joints in thick conducting screens," *IEEE Trans. Ant. Prop.*, vol. AP–36, 2, pp. 247–257, Feb. 1988.

[8] D.E. Merewether and R. Fisher, "Finite difference solution of Maxwell's equation for EMP applications," Electro Magnetic Appl., Inc., Report: EMA–79–R–4, Albq., NM, April 22, 1980.

[9] K.S. Cho and D.E. Merewether, "Thin-gap formalism in three dimensional rectangular coordinates," Electro Magnetic Appl., Inc., Tech. Rept. EMA–86–R–05, Albuquerque, NM, Dec. 1985.

[10] K.S. Yee and J.C. Kasher, "Modeling the electromagnetic coupling through small circumferential seams with FDTD," Lawrence Livermore National Lab. Tech. Report, UCRL–97239, Livermore, CA, Aug. 1987.

[11] D.J. Riley and C.D. Turner, "Hybrid thin-slot algorithm for the analysis of narrow apertures in finite-difference time-domain calculations," *IEEE Trans. Ant. Prop.*, vol. AP–38, 12, pp. 1943–1950, Dec. 1990. See also Sandia National Laboratory Tech. Rept. SAND89–3073, Albuquerque, NM, Jan. 1990.

[12] H.H. Chao and B.J. Strait, "Computer programs for radiation and scattering by arbitrary configurations of bent wires," Scientific Rept. 7, Contract F19628–68–0180, AFCRL–700374, Sept. 1970.

[13] J. Moore and R. Pizer, Eds., *Moment Methods in Electromagnetics*, Research Studies Press Ltd., Letchworth, England, 1984.

[14] A.J. Julian, J.C. Logan, J.W. Rockway, "Mininec: a mini-numerical electromagnetics code," Naval Ocean Systems Center, Tech. Doc 516, San Diego, CA, Sept. 1982.

[15] J.A. Landt, E.K. Miller, M. VanBlaricum, "WT–MBA/LLL1B: A computer program for the time-domain electromagnetic response of thin-wire structures," Lawrence Livermore National Laboratory, Tech. Rept. UCRL–51585, May 1974.

[16] R.A. Dalke, "A numerical method for the analysis of coupling to thin-wire structures," Symposium Record, Int. Symp. on Electromagnetic Comp., pp. 55–61, Seattle, Wash., Aug. 1988.

[17] E.K. Reed and C.M. Butler, "Electromagnetic penetration through narrow slots in conducting surfaces and coupling to structures on the shadow side," Clemson University Tech. Rept. TR–062188–3273F2, Clemson, SC, Aug. 1990.

[18] L.K. Warne and K.C. Chen, "Equivalent antenna radius for narrow slot aperture having depth," *IEEE Trans. Ant. Prop.*, vol. AP–37, 7, pp. 824–834, July 1989.

[19] L.K. Warne and K.C. Chen, "Slot aperture having depth and losses described by local transmission line theory," AFWL Interaction Note 467, Air Force Weapons Laboratory, Albq. NM, June 1988.

[20] R.W. Lyon and A.J. Sangster, "Efficient moment method analysis of radiating slots in a thick-walled rectangular waveguide," *Proc. IEE*, Vol. 128, 4, Aug. 1981.

[21] E.L. Coffey and D.L. Kadlec, "GEMACS Version 4, User and engineering manuals," Rome Air Development Center, Tech. Rept. RADC–TR–87–68 (vol. 1 of 3), Griffiss Air Force Base, NY, May 1987.

[22] D.J. Riley and C.D. Turner, "The inclusion of wall loss in electromagnetic finite-difference time-domain thin-slot algorithms," Sandia National Laboratories Tech. Report, SAND90–2091, Albuquerque, NM, Sept. 1990.

[23] D.J. Riley, C.D. Turner, L.D. Bacon and J.D. Kotulski, "Numerical modeling tools for transient electromagnetic problems," Sandia National Laboratories Tech. Report, SAND90–0519, Albuquerque, NM, April 1990.

DISTRIBUTION:

Phillips Laboratory
Kirtland Air Force Base
Albuquerque, NM 87117–6008
W. Baker, PL/WSE (1)
P. Vail, PL/WSM (1)
T. Timmerman, PL/WSMM (5)

Defense Nuclear Agency Headquarters
6801 Telegraph Rd.
Alexandria, VA 22310–3398
Attn: Dr. G. Baker, DNA/RAEE (1)

EMA
5101 Copper Av. NE., Suite 201
Albuquerque, NM 87108
Attn: Dr. D.E. Merewether (1)

General Dynamics–Pamona
401–01
P. O. Box 507
Pamona, CA 91769
Attn: R. McDonald (1)
K. Brown (1)

Harry Diamond Laboratory
2800 Powder Mill Rd.
Adelphi, MD 20783–1197
Attn: L. F. Libelo (1)
J. Tatum (1)
E. Brown (1)

JAYCOR
39650 Liberty St.
Suite 320
Fremont, CA 94538
Attn: Dr. K. Casey (1)

Kaman Sciences/Dikewood Division
2800 – 28th St., Suite 370
Santa Monica, CA 90405
Attn: Dr. K.S.H. Lee (1)

Kaman Sciences
P. O. Box 7463
Colorado Springs, CO 80933
Attn: L. Allen (1)

Rome Air Development Center
RL/RBCT
Griffiss AFB, NY 13441
Attn: A. J. Pesta (1)

Lawrence Livermore National Laboratory
University of California
P. O. Box 808
Livermore, CA 94550
Attn: D. Goerz, L–156 (1)
S. L. Ray, L–156 (1)
H. Cabayan, L–86 (1)
R. Mcleod, L–156 (1)
S. Nelson, L–156 (1)
R. Zacharias, L–153 (1)

Los Alamos National Laboratory
University of California
P. O. Box 1663
Los Alamos, NM 87545
Attn: E.K. Miller, MS–J580 (1)
T. Kwan, MS–B259 (1)
B. Schafer, MS–C931 (1)

Naval Research Laboratory
4555 Overlook Ave. SW
Washington, D. C. 20375–5000
Attn: A. W. Ali (1)
W. M. Manheimer (1)
T. J. Wieting, Code 4650 (1)

U. S. Army Vulnerability Assessment Laboratory
White Sands Missile Range, NM 88002–5513
Attn: L. Gomez (1)

Virginia Polytechnic Institute
Dept. of Electrical Engineering
Blacksburg, VA 24061
Attn: Dr. W. A. Davis (1)

Syracuse University
Dept. of Electrical and Computer Engineering
Syracuse, NY 13210
Attn: Dr. T. K. Sarkar (1)

Clemson University
Dept. of Electrical and Computer Engineering
Clemson SC 29634–0915
Attn: Dr. C. M. Butler (1)

Northwestern University
Technological Institute
Dept. of Electrical Engineering and Computer Science
Evanston, IL 60201
Attn: Dr. A. Taflove (1)

Lockheed Missiles and Space Co.
Sunnyvale, CA 94086
Attn: Dr. K. S. Yee (1)

EMA
P.O. Box 260263
Denver, CO 80226
Attn: Dr. J.E. Elliott (1)

Computer Sciences Corporation – Systems Division
2100 Air Park Road, SE, Suite 200
Albuquerque, NM 87106
Attn: Dr. R.W. Holland (1)

University of Dundee
Department of Mathematical Sciences
DUNDEE DD1 4HN
Scotland, UK.
Attn: Dr. Paul D. Smith (1)

FGE Ltd.
Miltons
Petworth Road, Witley
Godalming, Surrey
GU 8 5LH
UK
Attn: Dr. Alec Milne (1)

Sparta
4901 Corporate Dr.
Huntsville, Al 35805
Attn: Dr. Robert E. O'Conner (1)

University of Arizona
Dept. of Electrical Engineering
Tucson, AZ 85721
Attn: Dr. D. G. Dudley (1)

University of Houston
Dept. of Electrical and Computer Engineering
Houston, TX 77004
Attn: Dr. D. R. Wilton (1)

BDM Corporation
1801 Randolph Road
Albuquerque, NM 87106
Attn: Dr. R. J. Antinone (1)

Pennsylvania State University
Department of Electrical Engineering
University Park, PA 16802
Attn: Dr. K.S. Kunz (1)

New Mexico State University
Department of Electrical Engineering
Box 30001, Dept. 3–0
Las Cruces, NM 88003–0001
Attn: Mr. R. Jedlicka (1)

JAYCOR
P.O. Box 3980
Santa Barbara, CA 93130
Attn: Dr. B. Crevier (1)

Internal Distribution:

1244 J. M. Hoffman
1244 L. D. Bacon
2343 B. C. Brock
3141 S. A. Landenberger (5)
3145 Document Processing (8)
For DOE/OSTI
3151 G. C. Claycomb (3)
7553 M. E. Morris
7553 L. K. Warne
7553 K. O. Merewether
7553 T. E. Koontz
7555 G. Seely
8523 R. C. Christman (1)
9300 J. E. Powell
9350 J. H. Renken
9351 E. F. Hartman
9352 G. J. Scrivner
9352 C. D. Turner (6)
9352 C. N. Vittitoe
9352 D. J. Riley (20)

*U.S. GOVERNMENT PRINTING OFFICE 1991-0-573-038/44036